Tectonics®

Key Points:

- Metamorphic veins are rheological heterogeneities capable of localizing deformation within the rock volume
- (Ultra)cataclasites and breccias are inferred to have formed at blueschist-facies conditions; blueschists deformed by brittle and pressure-solution creep mechanisms
- Brittle fabrics are associated with the injection of externally derived fluids at depths compatible with slow slips and tremors

Correspondence to:
J. Muñoz-Montecinos,
jmunoz@erdw.ethz.ch

Shattered Veins Elucidate Brittle Creep Processes in the Deep Slow Slip and Tremor Region

J. Muñoz-Montecinos[1,2,3] , **S. Angiboust[1,4]** , **A. Garcia-Casco[2,5]** , **and T. Raimondo[6]**

[1]Institut de Physique du Globe de Paris, CNRS, Université Paris Cité, Paris, France, [2]Department of Mineralogy and Petrology, Faculty of Sciences, University of Granada, Granada, Spain, [3]Department of Earth Sciences, Structural Geology and Tectonics Group, Geological Institute, ETH Zürich, Zürich, Switzerland, [4]Laboratoire de Géologie de Lyon, Ecole Normale Supérieure de Lyon, Lyon, France, [5]Instituto Andaluz de Ciencias de la Tierra, CSIC-Universidad de Granada, Granada, Spain, [6]UniSA STEM, University of South Australia, Adelaide, SA, Australia

Abstract Deep Slow Slip and Tremors (SSTs) are a combination of transient clusters of tectonic tremors and slow slip associated with extremely elevated fluid pressures. SSTs are thought to reflect a transition from viscous to brittle plate interface rheology and likely exert a first-order control on megathrust seismicity. Nevertheless, the deformation mechanisms governing the source of SSTs remain elusive. We herein document the occurrence of vein networks precipitated and brecciated within the deep SST region under blueschist-facies conditions. These lawsonite-rich vein sets exhibit extensive evidence of brittle deformation and are spatially related to localized, finely milled (cataclastic) shear bands. Petro-geochemical data reveal that brittle deformation was accompanied by the injection of several ultramafic-, mafic- and metasedimentary-derived fluid pulses, imprinting characteristic Cr, high field strength elements, and light over heavy rare earth elements positive anomalies in the vein breccias while leaching light rare earth elements from the cataclastic blueschist host. Our results suggest that metamorphic veins represent zones of mechanical anisotropy within the rock volume prone to localized shearing, brittle deformation and episodic injection of externally derived fluids. These networks demonstrate the importance of former vein sets as structural heterogeneities in triggering fluid-controlled brittle creep events. The combined effects of high pore fluid pressures and rheological heterogeneities in the form of metamorphic veins could trigger the nucleation and propagation of SSTs at the margins of this mechanically anisotropic environment, and thus determine where slip will take place along deep subduction interfaces.

Plain Language Summary The discovery of "slow" earthquakes that occur at such slow velocities that are imperceptible to human senses but can be measured instrumentally has generated a number of questions regarding the rheological behavior of subduction zones. A key approach to gain valuable information about these phenomena is by studying metamorphic rocks that were once buried, and subsequently exhumed, to and from depths at which these slow earthquakes occur. In this paper we study the structures that record the deformation of these rocks. We report a diversity of structures, among which are veins that are made of minerals that behave as rigid objects, while the surrounding rock matrix behaves in a viscous manner. We note that evidence of brittle and shear deformation is found mainly in these veins and in the rock immediately surrounding them. These brittle deformation events would have been triggered by the contrast in mechanical properties between the veins and their host rock, as well as by the injection of fluids at high pressures. These structures exhibit characteristics that can be compatible with some of these slow earthquakes, shedding light on their formation source processes.

1. Introduction

The discovery of deep Slow Slip and Tremors (SSTs; Rogers & Dragert, 2003) represented a major milestone for understanding the megathrust seismic cycle and plate interface rheology. SSTs consist of aseismic slow slip events (SSEs) and tremor swarms (low- and very-low-frequency earthquakes; LFEs), commonly occurring down to 60 km depth (Brown et al., 2009; Fu & Freymueller, 2013). In deep subduction environments, SSEs and LFEs are characterized by slip velocities of c. 10^{-8} m/s and c. 10^{-4}–10^{-3} m/s, respectively, and occur in patches at the tens of meters to hundreds of kilometers, with durations ranging from minutes to years (Behr & Bürgmann, 2021; Bostock et al., 2015; Ide et al., 2007; Shelly et al., 2006). Minimum stress drops (<100 kPa; e.g., Rubin & Armbruster, 2013; Shelly et al., 2006) demonstrate that the subduction interface or its surroundings generally fail
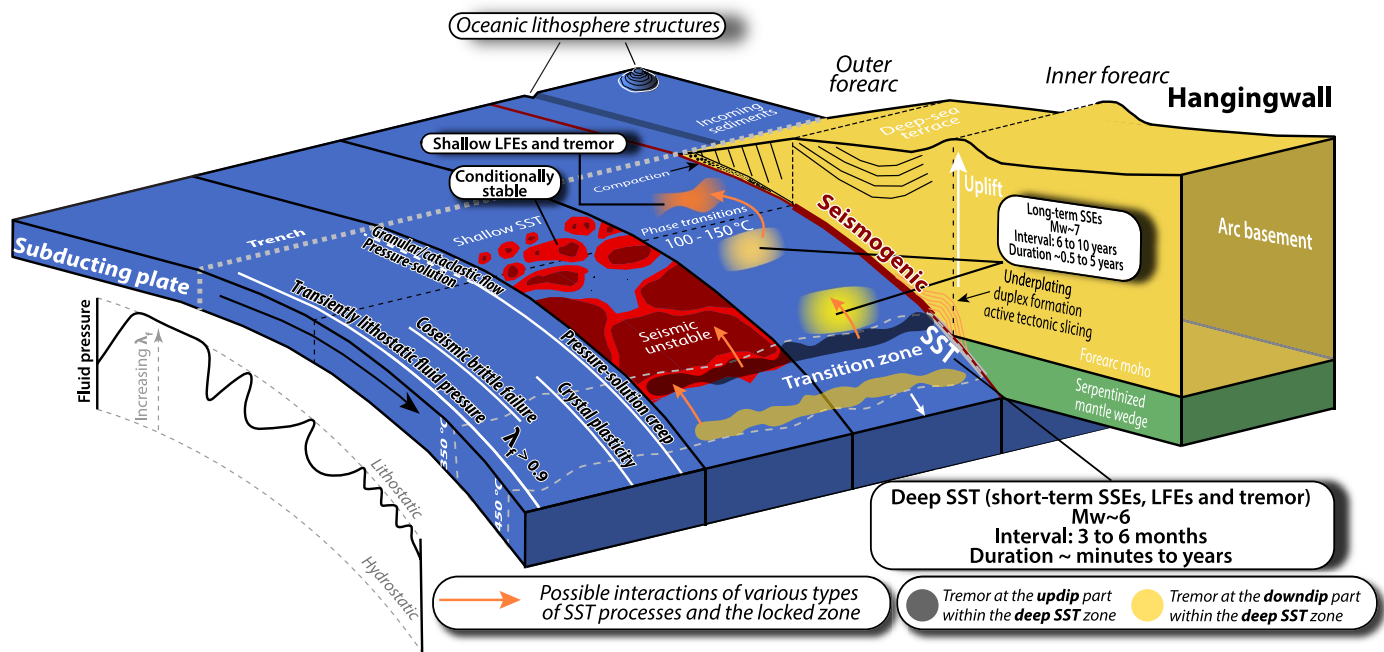
Figure 1. Along-dip frictional segmentation in subduction zones. Schematic overview of the various earthquake phenomena, their general properties and interactions between them (inspired by Bassett and Watts (2015) and Obara and Kato (2016)). Major deformation mechanisms as well as along-dip variations of the pore fluid pressure state are also depicted (modified from Oncken et al. (2022) and references therein). LFEs–low-frequency earthquakes; SSEs–slow slip events; SST–episodic tremor and slip; λ_f–pore fluid pressure factor (calculated as the ratio between the fluid pressure and the lithostatic load).

at very low differential stress. Local and far-traveled seismic activity could trigger SSTs in remote locations, as can Earth's tide stress modulations (Fry et al., 2011; Thomas et al., 2009). The spatial and temporal distribution of deep and shallow SSTs suggest that they might interact with the seismogenic region (where large megathrust earthquakes nucleate), likely building up stresses preceding co-seismic slip (Figure 1; Obara & Kato, 2016).

Highly electrically conductive layers and high compressional-to shear-wave velocity ratios (Vp/Vs) are commonly interpreted as near-lithostatic pore fluid pressure conditions along the plate interface (Audet & Kim, 2016; Delph et al., 2018; Wannamaker et al., 2014). Spatial-temporal SST variations as well as focal mechanisms suggest episodic fluid circulation (Warren-Smith et al., 2019), which in turn involves cyclic fluid overpressures, analogous to the fault-valve behavior (Gosselin et al., 2020) originally proposed for crustal faults (Sibson et al., 1988). Such fluids are most likely derived from metamorphic dehydration reactions affecting the subducting oceanic lithosphere (Peacock, 2009). Thus, the megathrust could be regarded as a high permeability conduit (at least transiently), sandwiched between the lower permeability overriding plate and the oceanic lithosphere, capable of channelizing fluid pulses updip and along strike (Cruz-Atienza et al., 2018; Dal Zilio & Gerya, 2022; Frank et al., 2015; Hyndman et al., 2015). Although most tectonic tremors are considered as the result of brittle shearing (Bostock et al., 2015), the apparent mismatch between scaling relationships, such as source duration and magnitude, led Shapiro et al. (2018) to speculate that extensional fracturing (hydrofracturing) can well explain LFE source properties.

Novel experimental, numerical, and geological investigations have attempted to characterize the deformation mechanisms associated with SST-related phenomena by inferring a match between transient deformational and geophysically observed patterns (Angiboust et al., 2015; Beall et al., 2019; Giuntoli & Viola, 2022; Kotowski & Behr, 2019; Leeman et al., 2016; Tarling et al., 2019). By using the constitutive flow laws of dislocation creep, solution-precipitation creep and brittle creep, Oncken et al. (2022) demonstrate that the entire spectrum of instrumentally observed SST strain rates could be accommodated by brittle creep, whereas pressure-solution creep is expected to dominate during seismic loading and background plate convergence rates. At depth (e.g., blueschist-facies conditions), (ultra)cataclastic networks are increasingly recognized as a likely product of several SST-related processes (Angiboust et al., 2015; Fabbri et al., 2020; Oncken et al., 2022) and mantle wedge seismicity (Angiboust et al., 2021). Other lines of geological evidence have also speculated on the potential
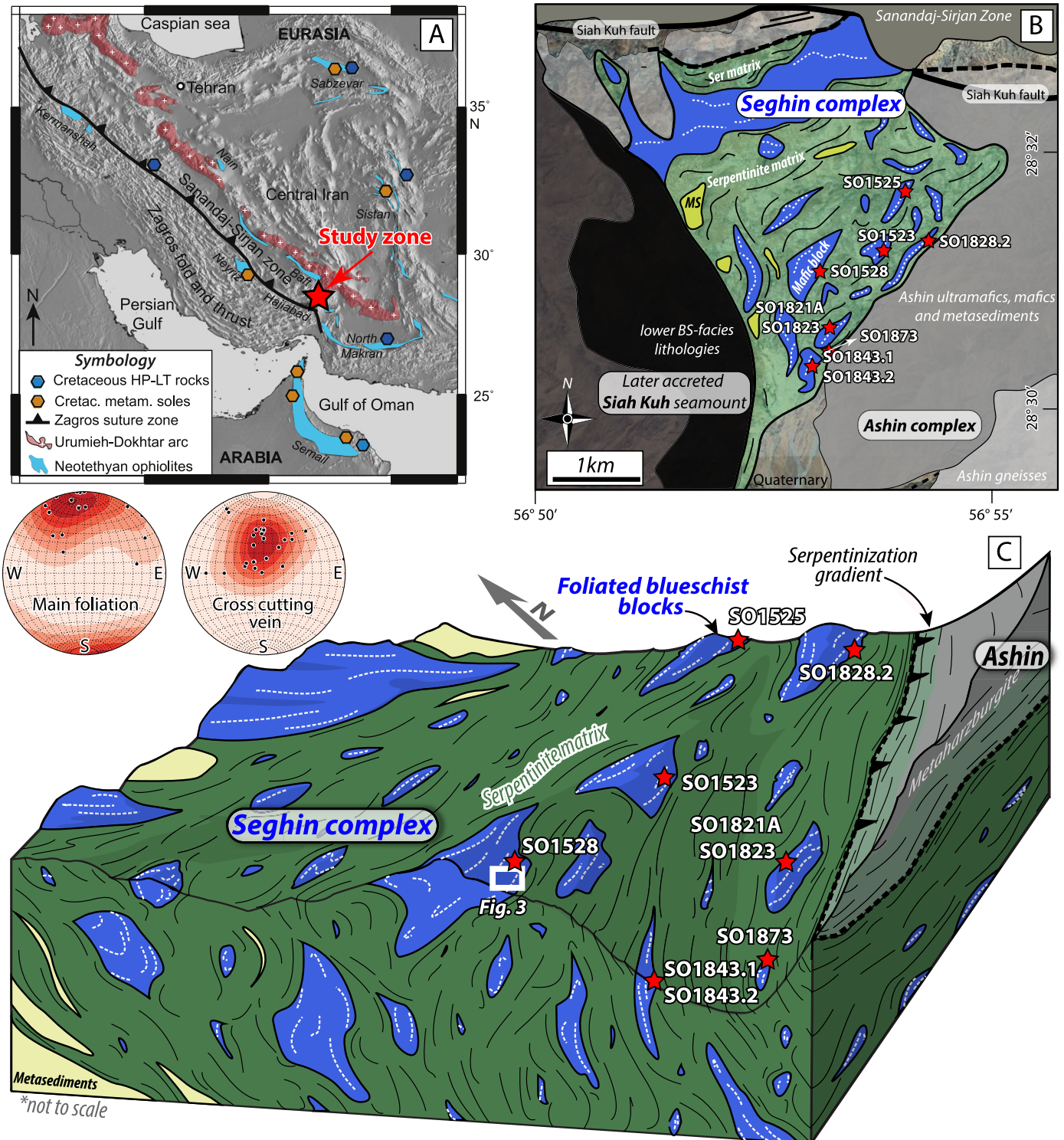
contribution of crystal plasticity or diffusion-dominated deformation mechanisms to the SST process (e.g., Giuntoli et al., 2022; Kotowski & Behr, 2019). Consequently, exhumed bodies of subducted metamorphic rocks and finite deformation patterns therein are particularly well suited to assess the transient nature of SSEs and LFEs (Behr & Bürgmann, 2021). Some of the typical rock features observed include (a) distributed viscous flow in a weak matrix coeval with brittle deformation of stiffer blocks (Fagereng & Sibson, 2010; Kotowski & Behr, 2019); (b) veins exhibiting evidence of re-opening and re-precipitation (Fagereng et al., 2010; Ujiie et al., 2018); (c) brittle creep localized into shear zones (Angiboust et al., 2015; Oncken et al., 2022; Rowe et al., 2011); and (d) metamorphic reactions indicative of the transition from viscous to brittle rheology (Tarling et al., 2019). In most cases, it has been inferred that these mechanisms acted in the presence of overpressurized fluids in order to promote brittle deformation. Such fluids decrease the effective normal stress acting on the shear zone and mobilize dissolved solutes released during pressure-solution creep. Despite this, no consensus exists regarding how the variety of SST-related phenomena are represented in outcrop, as emphasized in recent review works (Behr & Bürgmann, 2021; Kirkpatrick et al., 2021; Oncken et al., 2022). Primarily, understanding the physical processes during each incremental slip event, perhaps on the order of several microns (Williams & Kirkpatrick, 2022), remains challenging because key structures record a long-lived sequence of events and are commonly subject to obliteration and re-crystallization during further metamorphism and exhumation.

We herein provide new geological observations illuminating the deep SST source by investigating the deformation of high pressure-low temperature (HP-LT) metamorphic veins and their blueschist host. We document the first in situ occurrence of brecciated lawsonite-rich vein systems and associated (ultra)cataclasites, both inferred to have precipitated and deformed along the plate interface at depths compatible with SSTs (c. 30–55 km). Our petrological-structural approach aims to (a) characterize deformation mechanisms and metasomatic fingerprints recorded by cataclastic vein breccias and their surroundings; (b) provide geological observations suggesting brittle creep as a major deformation mechanism in the deep SST region; and (c) propose a comprehensive model linking the observed vein formation, brittle and viscous deformation and fluid flow events in light of the geophysical properties of deep LFEs and SSEs.

2. Geological Context

The Zagros suture zone in southeastern Iran (Figure 2a), and more specifically in the Soghan region (Figure 2b), contains the remnants of the southern Neo-Tethyan oceanic lithosphere inherited from the Lower Cretaceous to Eocene subduction event between Eurasia and Arabia. This pile of variably metamorphosed tectonic slivers, now exposed as an antiformal nappe-stack (Angiboust et al., 2016; Ghasemi et al., 2002), was accreted against the Sanandaj-Sirjan Zone upon subduction and subsequent collision (SSZ; Agard et al., 2006 and references therein). The SSZ comprises Jurassic to Eocene arc-related magmatic rocks (e.g., Alavi, 1994; Kananian et al., 2014), along with Mesozoic to Paleozoic high temperature gneisses. This lithological association is widely regarded as the upper plate of the continental southwestern margin of Eurasia (Agard et al., 2006; Arvin et al., 2007; Hassanzadeh & Wernicke, 2016). Unlike the SSZ, Soghan region lithologies exhibit a well-marked blueschist-facies metamorphic overprint (Agard et al., 2006; Oberhänsli et al., 2007; Sabzehei, 1974). Petro-chronological investigations point to a long-term cooling—at least from c. 115 to 60 Ma—of the subduction thermal structure from 18 down to 7°C/km. The Ashin complex, inferred to have been first subducted under a high thermal gradient (amphibolite-facies), has been partly overprinted by a lawsonite-blueschist-facies imprint during this long-term cooling and subsequent juxtaposition with the underlying Seghin and Siah-Kuh complexes (Angiboust et al., 2016; Bonnet et al., 2020; Holtmann et al., 2022).

Because of its relevance to deep subduction processes, as well as the excellent degree of preservation of the blueschist-facies mineral assemblage, we focus in this work on the Seghin complex. This tectonic sliver consists of a tectonic mélange, where up to hectometer-sized lawsonite-bearing blueschist blocks with metamorphic veins are wrapped by a serpentinite-rich matrix (variety antigorite; Figure 2c; see further geological details in Angiboust et al. (2016) and Muñoz-Montecinos, Angiboust, Garcia-Casco, Glodny, and Bebout (2021)). This macro-scale fabric exhibits a pervasive main foliation oriented to the northeast dipping from sub vertical (mostly in the blueschist blocks) to sub-horizontal. In general, the long axis of the blocks coincides with the general elongation vector of the complex that is generally oriented to the NNE-ENE. Metasediments, including marbles, metapelites and calcschists, are minor (making up to c. 5 vol% of the complex) and occur as blocks within the serpentinite matrix or as fine interlayering within the blueschists. However, they become significantly more

Figure 2. Geological context. (a) Simplified regional geological map of the Zagros suture, Iran, depicting the studied locality in the Soghan region (modified from Holtmann et al. (2022)). (b) Simplified geological map of the study locality (Soghan region, Southern Iran), depicting the structural fabric (block-in-matrix) of the Seghin complex (modified from Angiboust et al. (2016)). Blueschists, metasediments (MS) and serpentinites are displayed in blue, yellow and green colors, respectively. (c) Geological sketch of the present-day Seghin complex fabric (after Muñoz-Montecinos, Angiboust, Garcia-Casco, Glodny, & Bebout, 2021). Red stars indicate sample locations (see Appendix 1 of Supporting Information S1 for full details). The lower hemisphere equal area stereographic projections depict main foliation and crosscutting vein attitudes.

abundant toward the base of the Seghin complex approaching the contact with the Siah-Kuh seamount (Angiboust et al., 2016). Peak metamorphic conditions have been estimated based on a chlorite-phengite multi-equilibrium thermobarometric approach along with the Raman Spectroscopy of Carbonaceous Material geothermometer, yielding pressure-temperature conditions in the range of 1.4–1.8 GPa and 400–520°C (Angiboust et al., 2016). Such metamorphic conditions (likely less than 7°C/km) have been confirmed applying further thermodynamic modeling approaches (Muñoz-Montecinos, Angiboust, Garcia-Casco, Glodny, & Bebout, 2021). Multimineral Rb-Sr geochronology yielded an age range of 75–62 Ma for the peak lawsonite-blueschist-facies metamorphism (Angiboust et al., 2016). The Seghin complex is structurally sandwiched between the Ashin and Siah-Kuh complexes and is limited by two well-defined tectonic contacts marking a sharp lithological contrast among the different complexes (see Agard et al., 2006; Bonnet et al., 2020; Ghasemi et al., 2002; Sabzehei, 1974 for further geological details).

3. Methods

More than 40 rock samples of lawsonite-bearing veins and their host blueschists were collected during several field missions conducted between 2014 and 2018. Standard thin sections (30 μm thick) were produced for all samples except those analyzed by electron back-scattered diffraction (EBSD) techniques (see below). After petrographic examination, we selected 9 representative samples containing the most pristine and easily identifiable features. The coordinates of the samples studied are shown in Table S1 in Supporting Information S1 and on a schematic geological map in Figure 1b.

We applied a range of analytical techniques to characterize their textures, microstructures and geochemistry, including scanning electron microscopy, electron probe microanalysis (EPMA), EBSD, cathodoluminescence (CL) and Laser Ablation–Inductively Coupled Plasma–Mass Spectrometry (LA-ICP-MS) trace element analysis (rasterized traverses and 2D maps). Full analytical details are provided in Appendix 1 of Supporting Information S1.

4. Characterization of the Vein Systems

The blueschists hosting the metamorphic vein systems are generally fine-to coarse-grained metatuffs and metalavas and display a penetrative foliation, which is locally overprinted by a crenulation cleavage. The main phases constituting the dominant fabric are fibrous to lozenge-shaped Na-amphibole (mostly magnesio-riebeckite and glaucophane) and lawsonite grains, along with Na-Ca-clinopyroxene (omphacite and aegirine-augite), epidote, quartz, phengite (Si = 3.55 to 3.72 atoms per formula unit), titanite and rare garnet. We note that epidote occurs as inclusions within lawsonite, as a prograde phase in the matrix of the blueschists and replacing lawsonite as a retrograde phase. Evidence for the early prograde stage was almost completely erased, although some Ca-amphibole cores and epidote, quartz and albite inclusions within lawsonite are still locally preserved. The main foliation is commonly characterized by an anastomosing mylonitic fabric, where dark seam fringes generally occur surrounding large and likely stiffer crystals such as lawsonite. Thus, this texture shows strain caps coated with Na-amphibole around these rigid objects. Minor pyrite grains develop strain shadows decorated with quartz (see Muñoz-Montecinos, Angiboust, Garcia-Casco, Glodny, & Bebout, 2021 for further details).

The blueschists exhibit three main veining stages: (a) an early albite-rich precipitation; (b) a prograde to near-peak blueschist-facies precipitation and deformation of lawsonite-bearing veins; and (c) a near-peak formation of massive aragonite-bearing hydraulic breccias (see Muñoz-Montecinos, Angiboust, Garcia-Casco, Glodny, and Bebout (2021) for a detailed characterization of these veining events). We herein focus on the HP-LT lawsonite-rich vein sets because they formed and deformed within the SST region and show widespread and unreported cataclastic shear fabrics (see below). The first albite-rich vein sets were likely produced from internal mineral dehydration at sub-greenschist- to incipient blueschist-facies metamorphic conditions (Muñoz-Montecinos, Angiboust, Garcia-Casco, Glodny, & Bebout, 2021). These veins are commonly oriented subparallel and oblique to the main foliation, either as extensional structures or as veins that have been rotated and parallelized according to the main foliation as a consequence of shearing (these type of shearing-related vein structures are hereafter referred to as transposed veins). Subsequently, HP-LT lawsonite-bearing veining events overprinted these existing structures (i.e., the albite-rich veins) as well as the blueschist host. In this case, the lawsonite-bearing veins occur as extensional structures that developed tabular crystal habit and infiltrated through the previous albite-rich veins

(i.e., re-opening former veins) and the blueschist host. The mineralogy of these lawsonite-bearing veins comprises lawsonite, Na-amphibole (mostly glaucophane and magnesio-riebeckite), Na-Ca-clinopyroxene (aegirine-augite and subordinate omphacite), quartz, titanite and minor apatite, Si-rich phengite (Si = 3.55 and 3.67 atoms per formula unit) and aragonite. This mineral assemblage is characteristic of lawsonite-blueschist-facies metamorphism, representing pressure-temperature conditions of c. 200–500°C and 0.8–2.0 GPa (e.g., 25–60 km depth; see e.g., Evans, 1990). The occurrence of trails composed of host-vein wall solid materials aligned parallel to the actual host-vein margin, along with oscillatory chemical zoning patterns in amphibole, suggest that veining and precipitation occurred in an episodic manner (Muñoz-Montecinos, Angiboust, Garcia-Casco, Glodny, & Bebout, 2021).

Lawsonite-rich veins occur either parallel (as extensional and/or transposed structures), crosscutting at c. 30–60° in sets of conjugated structures (see stereographic projections in Figure 2c), or perpendicular with respect to the main foliation of the blueschist host. The widths of these networks reach the tens of centimeters-scale (mostly in the 10–20 cm range), while their lengths are typically meter-sized until up to 10 m in occasional cases. Veins exhibit widespread evidence of extensional fracturing and precipitation as syntaxial mode veins (in the sense of Bons et al. (2012); e.g., Figure S1a in Supporting Information S1), and are characterized by euhedral, centimeter-sized tabular lawsonite crystals. After precipitation as extensional structures, subsequent shearing resulted in heavily transposed vein networks, which in turn have been brecciated (vein breccias; e.g., Figures 3a, 4a, and 4b). The process of vein transposition and incipient brecciation is illustrated in Figure S1 of Supporting Information S1. There, tabular lawsonite occur elongated perpendicular to a sharp host-vein margin (Figure S1a in Supporting Information S1). These prisms are then rotated and bended according to the sense of shearing (Figure S1b in Supporting Information S1). Further strain resulted in incipient brecciation and comminution of lawsonite, where the fibrous texture is erased and the blueschist host is dragged within the vein (Figure S1c in Supporting Information S1). In the vein breccias, lawsonite clasts are surrounded or transected by millimeter-wide localized shear bands containing abundant quartz and Na-amphibole (Figures 4a and 4b, and Figure S2a in Supporting Information S1). In addition, extensional vein networks are closely associated with localized shear bands crosscutting the main fabric of the blueschist host (Figure 3b). Reconstruction of disrupted lawsonite grain shapes suggest extension from a few millimeters to a few centimeters. In several cases, veins exhibit highly strained, centimeter-sized sigmoidal lawsonite clasts in a matrix of heavily micro-brecciated lawsonite fragments associated with quartz and Na-amphibole (Figure 4b). There, crystal shape reconstruction is not possible due to substantial shearing and fracturing. Similar cataclastic structures are observed preferentially in the surrounding blueschists toward the vein-host margins (e.g., Figure 4c).

Lastly, precipitation of aragonite + quartz (± phengite and ± Na-amphibole) occurred at near-peak conditions within the deepest PT region of the lawsonite-blueschist-facies in the form of hydraulic breccias crosscutting the previous extensional and transposed veins as well as the blueschist main foliation (see Muñoz-Montecinos, Angiboust, Garcia-Casco, Glodny, and Bebout (2021) for further details).

5. Microstructures of the Vein Breccias and Their Blueschist Host

The cataclastic blueschist is in contact with a heavily comminuted (ultra)cataclasite preferentially located in the host-vein margins (Figures 4c and 5a) and showing sharp slip surfaces. Epidote and lawsonite from the cataclastic blueschist exhibit evidence of brittle fracturing and grain rotation (Figure S2d in Supporting Information S1), indicating extension and displacements up to the millimeter-scale. The (ultra)cataclasite consists of high modal proportions of Na-amphibole and titanite, with subordinate lawsonite and rare epidote. Strain shadows around epidote clasts hosting chlorite and Na-amphibole are widespread. Furthermore, in the blueschist host, Na-amphibole grains are boudinaged and display glaucophane sealing the necks and rims, as well as the matrix around the boudins (Figure S2e in Supporting Information S1), pointing to HP-LT conditions for dissolution-precipitation processes after brittle creep. In the XY plane (with respect to the finite strain ellipsoid), shear planes or slickenlines (Figure 4d) coated with Na-amphibole fibers occur oriented parallel to the elongation orientation of the vein breccia fragments, assumed here to represent the X vector of the strain ellipsoid.

In the lawsonite vein breccias, the submillimeter-wide (ultra)comminuted shear bands are composed of Na-amphibole and titanite (e.g., Figures 5a and 5b). Highly sigmoidal Na-amphibole clasts are surrounded by a submicrometric cataclastic matrix (Figures 5c and 5d) exhibiting a crystallographic preferred orientation (CPO), where the [001] (<c>), [100] and [010] axes are oriented parallel to the elongation orientation, approximately
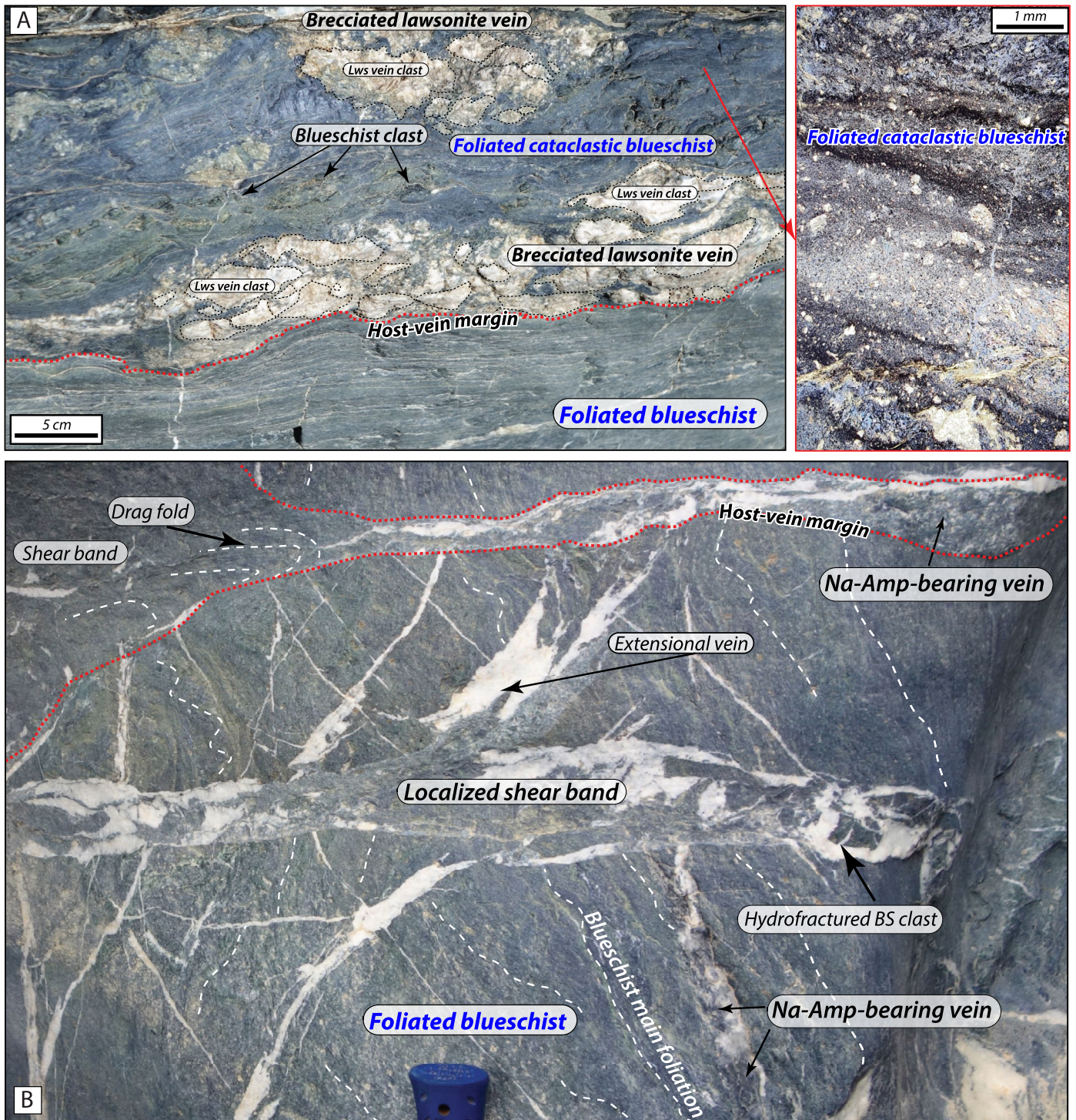
Figure 3. Meso-scale field view of a lawsonite vein breccia, a foliated cataclastic blueschist and their pristine host. A sharp fault trace separating the pristine and cataclastic domains is marked by a dashed red line. Note that the vein clasts show highly sigmoidal morphologies due to intense shearing. The inset depicts the general cataclastic micro-fabrics of the blueschists. (b) Outcrop view of an extensional vein system that evolved into a localized shear band (field of view, ~1 m).

perpendicular to it, and contained within the foliation plane, respectively (Figure 6a; see also Figure 6b). Interestingly, euhedral amphibole crystals hundreds of microns long occur bounding coarse-grained lawsonite vein breccia fragments (Figure 5e). In quartz bands wrapping lawsonite fragments (Figure S2b in Supporting Information S1; see also Figure 6d), quartz porphyroclasts are surrounded by dynamically recrystallized quartz aggregates
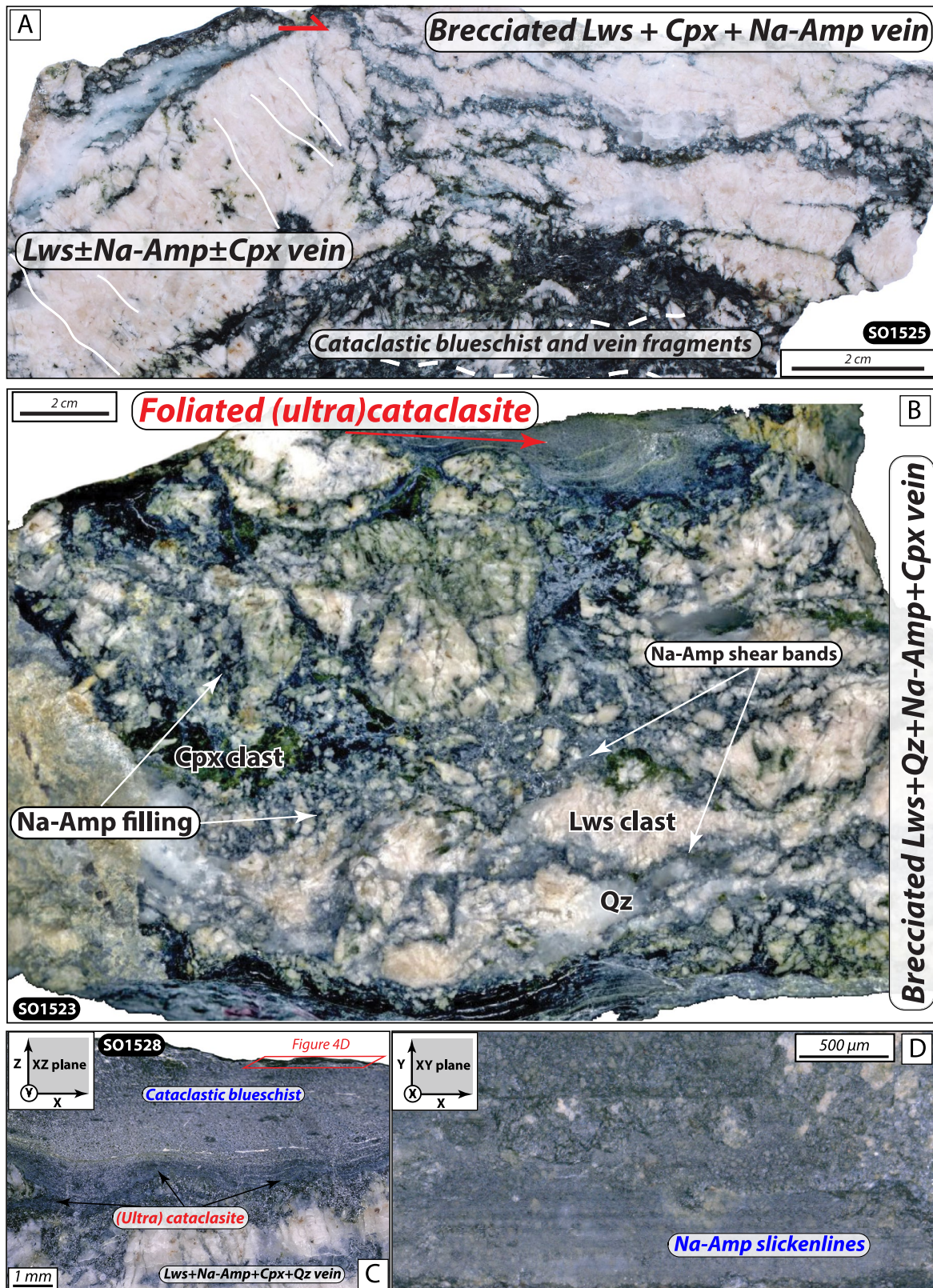
Figure 4.

with diameters smaller than 100 μm (mostly in the 15–50 μm range; Figure S4b in Supporting Information S1), defining core-and-mantle structures (Figures 5f and 5g). Moreover, sutured grain boundaries, bulging, rotated subgrains and dynamically recrystallized aggregates indicate crystal plasticity. The quartz <c> ([0001]) and <a> ([11$\bar{2}$0]) axes pole figures (Figure 6c) depict weak CPO maxima at c. 60° with respect to the stretching lineation and contained in the foliation plane, respectively, resulting from a simple shear regime (e.g., Morales et al., 2014). This pattern is highlighted in the Z axis EBSD orientation map (with X being the maximum elongation orientation of the strain ellipsoid; Figure 6d), which reveals a weak CPO of the quartz c axis ([0001]) oriented at relatively high angles with respect to the elongation direction (see also Figure 6c). Note that <c> axes also exhibit a girdle oblique to the foliation and elongation directions (Figure 6c).

We note that stripes of quartz grains misoriented with respect to the host porphyroclast are common (Figure 5f). CL imaging (Figure 5g) reveals similar textures, characterized by shades of red and dark red that define stripes of sigmoidal quartz crystals within a porphyroclast. In addition, large quartz crystals are notably misoriented with respect to their mean orientation and are generally surrounded by poorly misoriented grains (Figure S4a in Supporting Information S1). In the case of lawsonite, a CPO could not be identified due to the fragmented nature of these grains. In addition, lawsonite crystals are not significantly misoriented, with the higher misorientation angles matching regions of twins or incipient undulose extinction (Figure S4d in Supporting Information S1).

6. Major and Trace Element Distribution Patterns

In the vein breccias, lawsonite exhibits Ti + Fe-rich (up to 1.5 wt% TiO_2 and 3.6 wt% FeO) and Al-poor domains (Figure 7a and Figure S2f in Supporting Information S1). An exchange vector (e.g., Brady, 1975) of the type $TiFeAl_{-2}$ can thus be identified. Cr is noticeably zoned (Figures S2f and S3b in Supporting Information S1), as are Sr, high field strength elements (HFSEs) and light and heavy rare earth elements (LREEs and HREEs, respectively; represented here by the Ce/Yb ratio; Figure 7b, Figures S3b and S3c in Supporting Information S1). The lawsonite textural patterns are highly variable, ranging from (a) sharp boundaries within grains; (b) patchy zoning; and (c) concentric zoning to (4) healed fractures (see numbered arrows in Figure 7a). In the case of Cr, the zoning patterns are well visible in rims or as tiny grains of lawsonite, as if Cr-rich zones were cementing the vein breccia structures (Figures S2f and S3b in Supporting Information S1). Similarly, Na-Ca-clinopyroxene displays patchy zoning patterns containing about 1 wt% TiO_2 in core domains, whereas Cr_2O_3 shows no trend but reaches up to 0.3 wt% (Figure S2g in Supporting Information S1). The lawsonite breccia matrix is enriched in LREEs, HFSEs, Cr and Ni (Figures 7c and 7d; see also Figures S3d and S3e in Supporting Information S1); the distribution of these elements evokes sealed cracks. The cataclastic blueschist host contains virtually identical trace element abundances compared to those of the averaged pristine blueschist samples (Figure 7e). Toward the ultracataclasite-vein margin, depletion in LREEs is observed over two orders of magnitude, whereas HFSEs (Zr-Ta-Nb-Ti) and Cr concentrations are enriched by a factor of at least 2.2 (Ta) and up to 12 (Zr) (Figures 7e and 7f). Last, we note that HREEs patterns are identical in all domains.

7. Discussion

7.1. Deformation Mechanisms Accommodating Strain at Peak Conditions

The mechanical role of metamorphic vein systems and related fluids has been well documented in former shallow subduction environments (<20 km depth; e.g., Braden & Behr, 2021; Cerchiari et al., 2020; Dielforder et al., 2015; Fisher & Brantley, 1992; Ujiie et al., 2018). Yet, in the deep subduction interface region, only few

Figure 4. Polished rock blocks depicting meso-scale brittle structures in vein breccias and (ultra)cataclastic shear bands. (a) Hand specimen showing an extensional lawsonite vein characterized by centimeter-sized tabular lawsonite crystals (solid white lines to the left), and its brecciated lawsonite-rich vein counterpart (dashed white lines to the right). Note that within the brecciated domain, Na-amphibole-rich shear bands surround lawsonite fragments. We emphasize that the mineralogy of the host blueschist domain differs with respect to that of the vein breccia, the latter containing remarkably higher amounts of Na-amphibole, quartz and clinopyroxene. (b) Hand specimen displaying heavily brecciated, sigmoidal and stretched lawsonite and to a lesser extent clinopyroxene clasts in a fine-grained matrix of lawsonite and Na-amphibole. In this case, the former clast shapes (i.e., tabular crystal shapes precipitated within extensional veins), were completely disrupted owing to intense shearing and wearing. This vein breccia is in sharp contact with a foliated ultracataclastic domain (red arrow). (c) Hand specimen view oriented according to the XZ plane of the strain ellipsoid (X being the maximum elongation orientation as indicated by fragmented lawsonite clasts and the slickenline lineation). Note the occurrence of a cataclastic blueschist in sharp contact with an ultracomminuted domain toward the host-vein margin. The whitish material giving a "dusty" appearance is a polishing residue. (d) Detailed hand specimen photomicrograph (see panel C for image location). The field of view is oriented according to the XY plane of the finite strain ellipsoid, showing slickenlines coated with Na-amphibole crystals. Cpx, clinopyroxene; Lws, lawsonite; Na-Amp, sodic-amphibole; Qz, quartz.
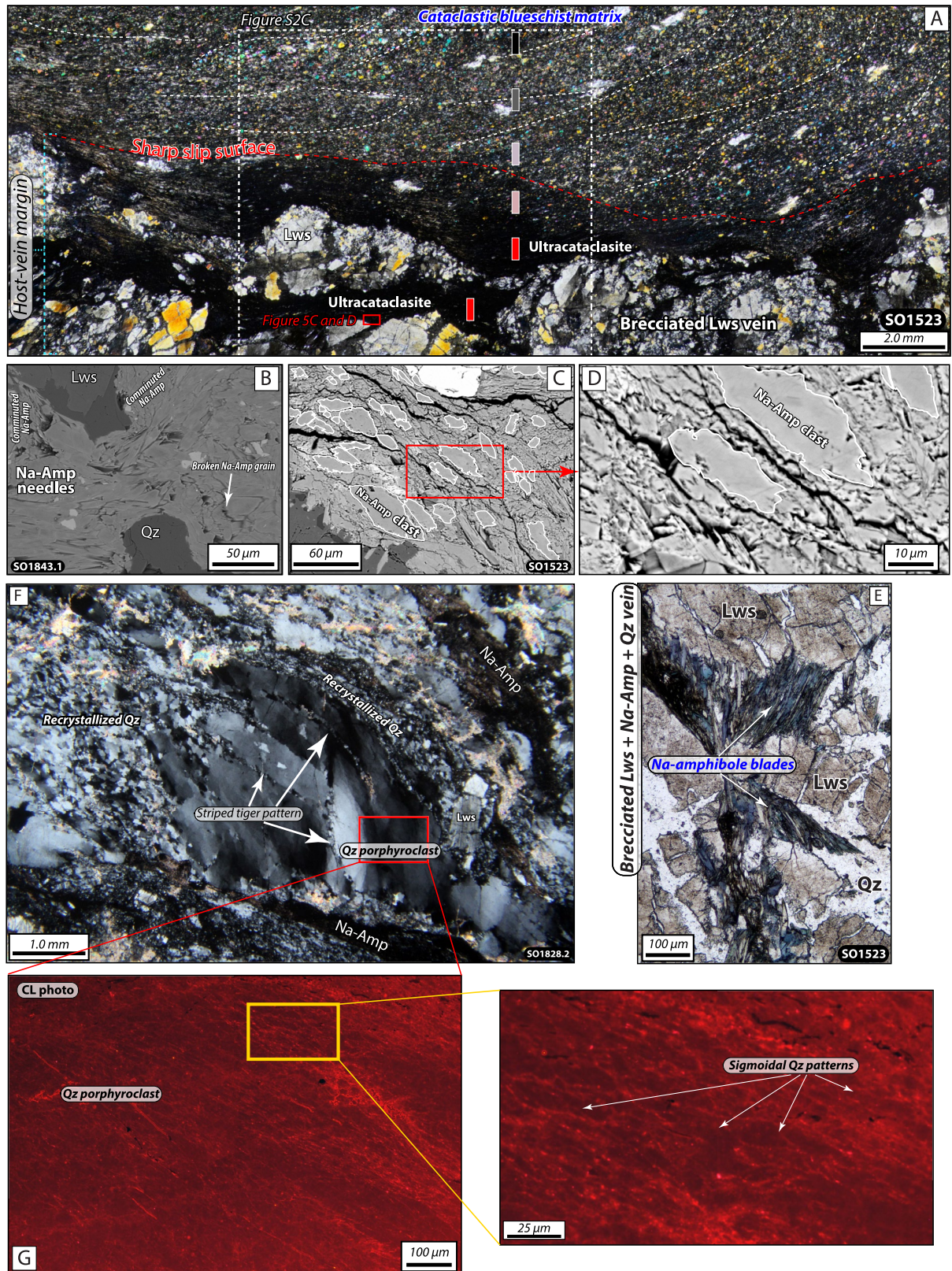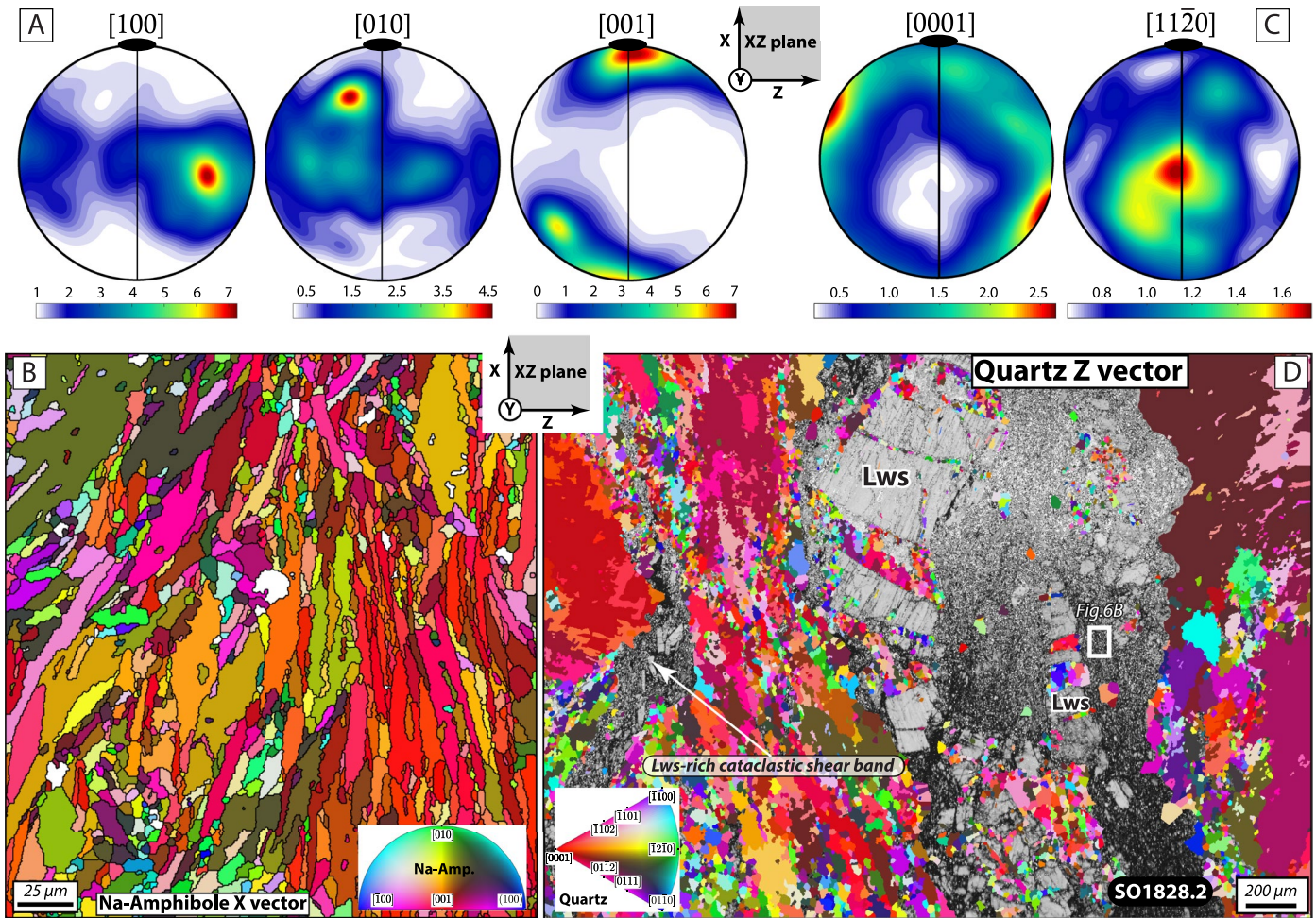
Figure 5.

Figure 6. Pole figures and Orientation maps of microstructures and fabrics in the vein breccias and (ultra)cataclasites. (a) Pole figure diagrams represented in an upper hemisphere equal area projection for Na-amphibole [100], [010] and [001] axes. (b) Orientation map (see location in panel (a)) colored according to the inverse pole figure key (IPF) of Na-amphibole (bottom right panel). View (*XZ* plane) corresponding to the *X* axis of the finite strain ellipsoid. (c) Pole figure diagrams represented in an upper hemisphere equal area projection for quartz [0001] (<*c*>) and [11$\bar{2}$0] (<*a*>) axes. (d) Orientation map colored according to the inverse pole figure key (IPF) of quartz (right panel). View (*XZ* plane) corresponding to the *Z* axis of the finite strain ellipsoid. Lws, lawsonite; Na-Amp, sodic-amphibole.

works—mostly from a geochemical perspective—have used vein systems as a proxy to illuminate fluid pathways and the deformation mechanisms therein recorded (e.g., Angiboust et al., 2017; Bebout & Barton, 1993; Giuntoli & Viola, 2022; Taetz et al., 2018).

Our results reveal that veins and their margins acted as zones of mechanical anisotropy in the rock volume as shown by (a) the intimate association between extensional and transposed vein networks, the latter being the

Figure 5. Structures, microstructures and fabrics of the vein breccias and (ultra)cataclasites. (a) Overview photomicrograph (crossed polars) of a cataclastic blueschist host and its vein margin. Strong grain size variation can be observed characterized by grain comminution from the cataclastic blueschist toward the ultracataclastic domains. The contact between the cataclastic blueschist and the ultracataclasite is sharply defined (red dashed line), whereas that of the ultracataclasite and the lawsonite vein breccia is diffuse. Note the strong mineralogical variation: epidote and lawsonite are abundant in the cataclastic blueschists, whereas the ultracataclasites largely comprise Na-amphibole and titanite. The red-black filled rectangles illustrate the rasterized surface dimensions (500 × 100 µm) and approximate distance from the vein toward the cataclastic host used for LA-ICP-MS trace element measurements as shown in Figures 7e and 7f; note that the rectangles do not show the actual along-foliation location of the analyzed surfaces. (b) Electron backscattered image of a Na-amphibole band from the vein breccia. The Na-amphibole crystals show acicular habit but are largely affected by comminution and brittle deformation, resulting in broken crystals. (c) Electron backscattered image (see red box in panel A for location) of a Na-amphibole shear band around a lawsonite porphyroclast. The amphibole clasts display highly sigmoidal morphologies surrounded by an ultracomminuted, submicrometric matrix. (d) Inset from panel C emphasizing the sigmoidal clasts and their ultracomminuted matrix. (e) Photomicrograph showing brecciated lawsonite crystals bounded by euhedral Na-amphibole blades. (f) Photomicrograph (crossed polars) of quartz from a lawsonite vein breccia depicting relevant microstructures explained in the main text. (g) Cathodoluminescence photomicrograph (CL photo) of a quartz crystal (see location in panel (f)) displaying in shades of dark red sigmoidal patterns not observed using the classical petrographic microscope, highlighted in more detail in the inset image.
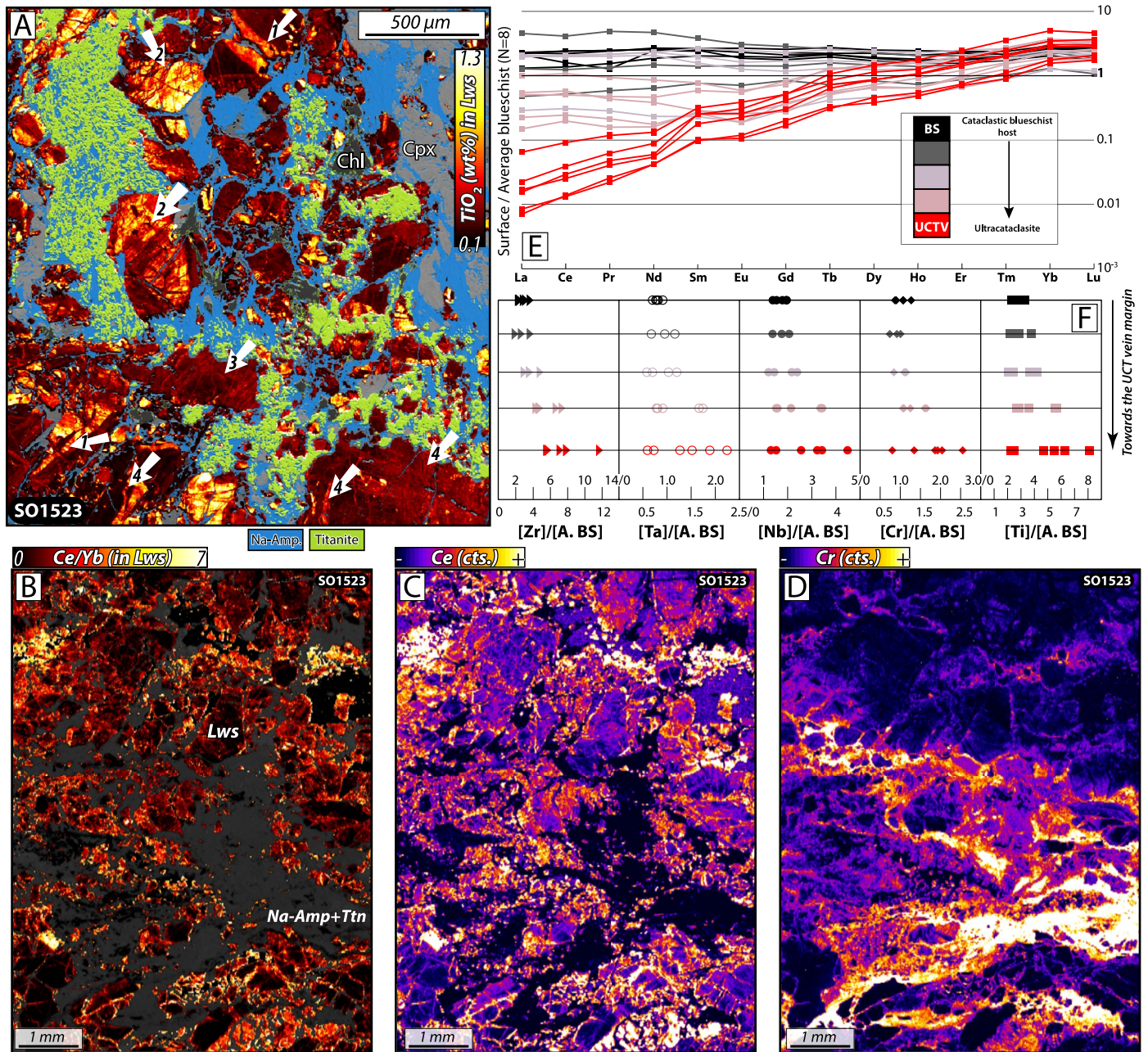
Figure 7. Vein breccia microtextures, fluid infiltration patterns and fault rock metasomatism. (a) Mask image based on high-resolution X-ray maps (WDS) over an electron backscattered image background. The blue and green colors of the mask indicate Na-amphibole and titanite, respectively, whereas the red-yellow colorscale corresponds to the TiO₂ wt% content in lawsonite. Arrows indicate zoning patterns described in the text: (1) sharp chemical zoning boundaries; (2) patchy zoning; (3) concentric zoning; (4) healed cracks. (b) Masked LA-ICP-MS maps over a greyscale image constructed from the sum of the analyzed major elements, highlighting Ce/Yb ratios in lawsonite. (c) LA-ICP-MS map showing the heterogenous distribution of Ce (in counts per second); note that the most enriched regions correspond to lawsonite grain boundaries, rims and healed cracks. (d) LA-ICP-MS map showing the distribution of Cr (in counts per second). The Cr-rich regions correspond to fluid pathways that crosscut all observed structures or percolate along grain boundaries, leading to tiny lawsonite rims or grains enriched in Cr as if they were cementing larger clasts (see also Figures S2f and S3 in Supporting Information S1). E-F. LA-ICP-MS rare earth element (La–Lu) and high field strength element (Zr, Ta, Nb, Cr, and Ti) composition diagrams of rasterized surfaces along a transect from the blueschist cataclastic matrix toward the ultracataclasite margin (red-black rectangles in Figure 5a), normalized to average pristine (i.e., non-cataclastic) blueschist compositions from Muñoz-Montecinos, Angiboust, Garcia-Casco, Glodny, and Bebout (2021). BS, blueschist; Chl, chlorite; Cpx, clinopyroxene; Lws, lawsonite; Na-Amp, sodic-amphibole; Ttn, titanite; UCT, ultracataclasites.

product of shearing-induced rotation of the former, and (b) the occurrence of extensional structures that evolved toward localized shear bands (e.g., Figures 3 and 4 and Figure S2a in Supporting Information S1). In addition, the diverse geometric arrangement of the vein network orientations thereby signals changes in the orientation of the principal stress (e.g., Cerchiari et al., 2020; Dielforder et al., 2015; Muñoz-Montecinos et al., 2020), in

agreement with geophysical observations monitoring the inversion of the stress field in active subduction margins as a consequence of the seismic cycle (Magee & Zoback, 1993; Sibson, 2013).

The occurrence of lawsonite vein breccias and localized shear bands containing (ultra)comminuted Na-amphibole (and titanite) crystals are evidence for a brittle creep process contributing to the finite deformation of these structures. Furthermore, the growth of Na-amphibole fibers elongated parallel to the general stretching orientation of the vein breccias along shear planes or slickenlines (e.g., Vignaroli et al., 2020) points to brittle deformation within the stability field of Na-amphibole (i.e., blueschist-facies). The Na-amphibole *X* axis orientation map (Figure 6b) highlights the CPO displayed in Figure 6a, where the [001] axis is oriented parallel to the elongation direction (see also the main text). This fabric has been documented in several geological and experimental investigations (Cao et al., 2014; Ildefonse et al., 1990; Kim et al., 2015; Kotowski & Behr, 2019; Park et al., 2020), and is considered as the product of cataclastic flow at high shear strains or confining pressures below 2.0 GPa, or as the result of dislocation creep. In our case, irrespective of their grain size, Na-amphibole crystals show no clear evidence of subgrains nor undulose extinction, suggesting that the Na-amphibole CPO cannot be explained by crystal plasticity.

Therefore, we infer that this fabric resulted from a rigid body rotation mechanism (Imon et al., 2004), similarly to the fabric displayed by lawsonite clasts. Widespread dissolution seams along with boudinaged and re-precipitated Na-amphibole grains in the host blueschists indicate, in turn, a viscous creep mechanism following brittle creep (Figures S2c and S2e in Supporting Information S1; Giuntoli et al., 2018; Misch, 1969; see also Muñoz-Montecinos, Angiboust, and Garcia-Casco (2021)). Pressure-solution and local dislocation creep along with fluid-derived precipitation may have contributed to the CPO visible in Na-amphibole shear bands (Imon et al., 2004), likely occurring at lower strain rates than the brittle events (Wassmann & Stöckhert, 2012). We note that coarse Na-amphibole blades occur sealing lawsonite vein clasts (Figures 5e and 7a). Such a texture indicates precipitation of minerals from a fluid phase in an open fracture (see Giuntoli and Viola (2022) for similar inferences in veins hosting carpholite fibers), which in turn suggests that former hydrofractures crosscut these cataclastic structures. Thus, the finding of mutual crosscutting relationships between cataclastic and extensional veins demonstrates that deformation and hydrofracturing occurred at near-lithostatic pore fluid pressure conditions. In consequence, our observations indicate that brittle creep and fluid overpressures acted coevally in the SST region, where pore fluid pressure above lithostatic likely produced hydrofracturing, while sub-lithostatic values, but close to the lithostatic threshold, enhanced localized brittle creep.

Based on our current understanding, the rates at which sealing occurred cannot be established because experimental investigations simulating crystal nucleation and growth in Na-amphibole-bearing hydrothermal systems have not been performed so far. However, we speculate that this process must have been rapid, possibly on the order of months or less. We stress that maintaining an open fracture filled with fluids and solutes at depths of 40–50 km is mechanically unfeasible, and only possible when the pore fluid pressure is lithostatic (e.g., Angiboust & Raimondo, 2022). In this case, hydrofracturing and subsequent shearing produce a negative feedback with the magnitude of the fluid pressure. Therefore, an increase in shear-enhanced permeability will dissipate the transient increases in pore fluid pressure (e.g., Saffer, 2014), as also inferred from geophysical observations suggesting permeability variations in the SST region at time scales in the order of months (e.g., Frank et al., 2015; Gosselin et al., 2020).

Only quartz displays firm evidence of crystal plasticity and thus can be considered as the weaker phase among the observed mineral assemblage. Interestingly, stripes of misoriented and apparently recrystallized grains occur crosscutting large porphyroclasts. Comparable textures are referred to in the literature as "striped tiger patterns" and are interpreted as resulting from strain hardening processes associated with a misoriented slip system with respect to the stress field (likely the <*a*> prism; Ceccato et al., 2017; Kjøll et al., 2015). Thus, after an incipient stage of crystal plasticity, the accumulation of dislocations (dislocation tangling) results in intra-granular fractures and micro-gouges (Menegon et al., 2008; Stünitz et al., 2003). We speculate that strain hardening resulted in brittle deformation of quartz followed by dislocation creep, in agreement with Na-amphibole and lawsonite cataclastic structures.

Similar fabrics have been documented for other lawsonite-bearing blueschists where the lawsonite crystals were deformed by rigid body rotation as stiff grains in a Na-amphibole-dominated matrix (Cao et al., 2014; Teyssier et al., 2010). We postulate that the lawsonite crystals deformed as brittle rigid particles within a quartz matrix,

the latter likely accommodating most viscous deformation after a stage of brittle creep. Therefore, the close relationship between cataclastic blueschists and lawsonite vein breccias confirms that (a) extensional veining generally preceded slip, and (b) the lawsonite vein-host rock margins acted as regions of mechanical anisotropy, thus localizing brittle creep within the rock volume. Although it was not possible to determine the precise number of slip events that produced the cataclastic fabrics, the discovery of several breccia generations as well as cross-cutting relationships between brittle fabrics, including the (ultra)cataclastic shear bands, points to repeated events of brittle fracturing, potentially in a cyclic manner.

7.2. Fluid Flow Associated With Cataclastic Deformation

We interpret the wide variety of observed mineral chemical zoning patterns, as well as the occurrence of sealed cracks, as a record of fossilized interstitial fluid pathways associated with episodic mineral precipitation from a fluid phase in an open system (see also Muñoz-Montecinos, Angiboust, Garcia-Casco, Glodny, & Bebout, 2021). Titanite and lawsonite typically contain negligible amounts of Cr unless the crystallizing medium (the fluid) is Cr-rich, with serpentinites being the most likely source of chromium (Spandler et al., 2011; Vitale Brovarone et al., 2014). Thus, the Cr enrichments in lawsonite veins and (ultra)cataclasites can be linked with the ingress of external fluids sourced from antigorite breakdown at greater, eclogite-facies depths (Angiboust et al., 2014; Padrón-Navarta et al., 2013; Spandler et al., 2011). Similarly, the high HFSE content and abundant titanite suggests crystallization from a HFSE-rich fluid (Liferovich & Mitchell, 2005). A comparable context is documented in the Tianshan belt (China), where the transformation of titanite into rutile and the devolatilization of hydrous phases during the blueschist-to-eclogite transition resulted in the mobilization of HFSEs into veins at the decameter-scale, but probably involving much larger distances (Gao et al., 2007). Similar conclusions regarding titanite and HFSE mobility were drawn from the Catalina Schists in California (Sorensen & Grossman, 1989), and in eastern Cuba for fluid-related jadeitite-forming processes in a paleo-mantle wedge setting (Cárdenas-Párraga et al., 2021). We therefore conclude that the fluids responsible for titanite crystallization and HFSE enrichment were derived from mafic lithologies near the blueschist-to-eclogite transition. Sr/Pb-rich patches (Figure S3b in Supporting Information S1) and high Ce/Yb ratios (Figure 7b) in lawsonite (or its healed cracks) further support episodic injection of mafic- or metasediment-derived fluids (Muñoz-Montecinos, Angiboust, Garcia-Casco, Glodny, & Bebout, 2021; Whitney et al., 2020).

The coeval development of veins, vein breccias and (ultra)cataclasites at the same metamorphic conditions offers a unique opportunity to illuminate the feedbacks between cataclasis and fluid flow, since ultracomminuted domains enhance metasomatism owing to larger reactive surface areas (Lai et al., 2015). Consequently, titanite enrichments associated with (ultra)comminuted materials may be interpreted as "metasomatic" records that depict slip events (seismic or subseismic) related to open-system fluid injection at subduction interfaces. This pattern is useful when analyzing deformation structures in rocks whose cataclastic fabrics have been obliterated during subsequent deformation (as in most cases). The observed LREE depletion toward the margin of the (ultra)cataclastic domain suggests preferential scavenging of trace elements around veins. Since epidote is a major LREE host (Tribuzio et al., 1996), we speculate that metasomatism enhanced by mechanical wearing in the (ultra)comminuted products of the host-vein margins boosted fluid-assisted leaching of epidote, mobilizing considerable amounts of LREEs.

7.3. Brittle Creep, Fluid Overpressures, and Weakening in the Deep SST Source

Evidence of brittle deformation is widespread along the lawsonite-rich veins and within the cataclastic blueschists adjacent to them (Figure 3), whereas the foliated blueschists away from these major structural heterogeneities are generally pristine and such brittle fabrics are scarce. Thus, we stress that the metamorphic veins-host rock margins documented here represent regions of mechanical anisotropy capable of localizing brittle shearing into discrete domains (e.g., Schrank et al., 2008). This effect is probably the result of the rigidity contrast between the lawsonite-rich veins (high rigidity objects) and the blueschist host.

Moreover, evidence of episodic reopening, such as crack-seals and mineral zoning patterns (e.g., Figure 7a), have been documented here suggesting that veins are structures capable of channelizing fluid flow (see Muñoz-Montecinos, Angiboust, Garcia-Casco, Glodny, & Bebout, 2021 for further details; see also Barker et al., 2006). Therefore, it is possible that high pore fluid pressure conditions localized—at least transiently—into

these high permeability conduits, might have contributed to the mechanical instabilities that resulted in brittle deformation near the host-vein margins. The vein breccias and (ultra)cataclastic blueschists were likely produced at subseismic strain rates (10^{-2} to $10^{-8}s^{-1}$; Fabbri et al., 2020; Rowe et al., 2011), faster than background plate convergence (on the order of $10^{-12}s^{-1}$). In the vein breccias, individual slip displacements were in the range of millimeters to a few centimeters, as inferred from lawsonite fragment geometry (e.g., Figures 4, 5a, and 6d). In addition, the occurrence of: (a) hundreds-of-microns long Na-amphibole blades precipitated from a fluid phase (Figure 5e), (b) extensional veins crosscutting the brecciated fabrics, and (c) metasomatism toward the vein margins, allow us to speculate that (a) shearing acted at near-lithostatic fluid pressures and (b) precipitation, clast dissemination and sealing occurred rapidly and, in consequence, so did extension.

Foliated ultracataclasites lining the host-vein interfaces, as well as shear bands within vein breccias, witness highly localized brittle shearing. These microstructures likely formed at the fastest strain rates compared to the rest of the structures reported in this study (e.g., Rowe & Griffith, 2015). Recently, Oncken et al. (2022) argued that LFEs would be localized into narrow principal slip zones in the order of millimeters to microns, while SSEs would also be confined to the same rock volume affected by brittle deformation. In consequence, we propose blueschist-facies ultracataclasites as a potential fossilized record of tremor-like signals and/or slow slips produced during SST events. Note that we cannot discard the possibility that other type of seismic events might have nucleated and/or propagated toward the deep subduction environment (e.g., Wang et al., 2020). Moreover, other deformation mechanisms could have acted synchronously and thus generate the finite deformation patterns that potentially represent the deep SST environment (Kirkpatrick et al., 2021).

Two mechanisms are invoked to drive slip from plate convergence toward subseismic rates. On the one hand, stress amplification or strain hardening due to rheological heterogeneities are both proven to trigger brittle deformation upon meeting certain conditions. For example, high ratios of stiffer materials with respect to a weaker matrix would cause slip acceleration toward subseismic rates (Beall et al., 2019), whereas at the crystal scale, strain hardening might trigger frictional sliding (Kjøll et al., 2015). On the other hand, high pore fluid pressures promote frictional sliding by decreasing the shear zone strength, hence enhancing strain rate bursts. Consequently, brittle creep and vein transposition could have been triggered by stress heterogeneities in a fluid-overpressurized environment. In fact, the former orientation of extensional veins with respect to the stress field affects their capability for deforming in a brittle manner (e.g., Figure 4a). For example, extensional veins formed and oriented parallel to the main compressive stress, σ_1, at a time t_0, might become favorably oriented for shearing at t_1 after rotation of σ_1 according to the seismic cycle (Figures 8a and 8b; e.g., Magee & Zoback, 1993; Meneghini & Moore, 2007; Muñoz-Montecinos et al., 2020; Sibson, 2013). Thus, structures favorably oriented for slipping may have ruptured in a brittle manner due to a complex interplay between stress heterogeneities (amplification), strain hardening and fluid overpressures. Once fractured and transposed, these structures become preferential weaknesses capable of deforming under a stress field misoriented for slipping (Figure 8c; Collettini et al., 2009; Fagereng et al., 2010). These structures are then ready for slipping, producing minor-amplitude stress drops as inferred for the weak SSTs source (Figure 8d; Shelly et al., 2006). Future numerical experiments should investigate the mechanical conditions required for enabling preferential fracturing of stiff materials in a weaker environment (Yamato et al., 2019).

The occurrence of a blueschist-facies foliation and widespread pressure-solution fabrics overprinting the cataclastic structures (Figure 5a, Figures S2c and S2e in Supporting Information S1) indicate that strength recovery is enhanced via dissolution-precipitation processes (e.g., Trepmann & Seybold, 2019). This allows cementation of the comminuted materials on short timescales, probably on the order of days to few weeks according to experimental investigations (e.g., Kay et al., 2006).

Quantifying the slipping surface or rupture length is critical for evaluating the potential of any geological object susceptible to SST-induced deformation (Behr & Bürgmann, 2021). Individual vein dimensions as seen in the field cannot explain source properties for SSEs and LFEs. Instead, the coalescence, rupture and simultaneous slip along numerous re-oriented vein networks may have generated events compatible with seismological observations, even though the magnitude of these events could not be determined. Furthermore, other geological objects representing rheological heterogeneities such as rigid blocks or lithologies (Behr et al., 2018; Kirkpatrick et al., 2021), in combination with deformed veins and (ultra)cataclasites (e.g., Angiboust et al., 2015), could have accounted for the SST-related finite deformation patterns potentially recorded here.

The wide range of inferred temperatures, fluid sources and flow length scales confirm that SSTs do not relate to any specific in situ metamorphic dehydration reaction (McLellan et al., 2022; Peacock, 2009). The vein breccias
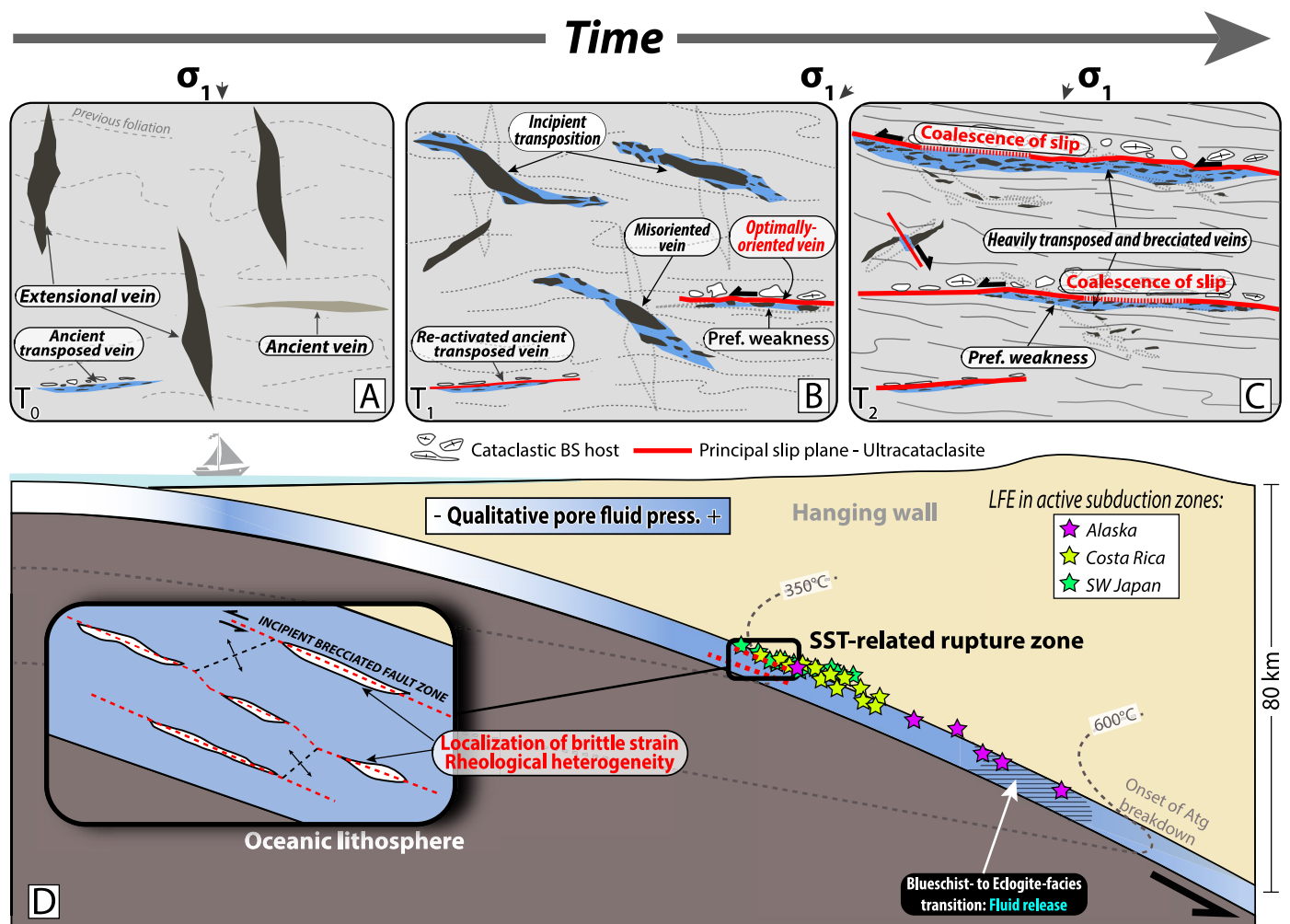
Figure 8. Formation and evolution of vein systems into preferential weaknesses, and principal slip zones in the Episodic Tremor and Slip source. Conceptual illustration depicting the main vein-forming and deformation processes associated with brecciated lawsonite veins and their (ultra)cataclastic host. This diagram is not intended to show a potential relation of the brecciated and cataclastic structures with large magnitude earthquakes nor time scales relevant for the seismic cycle, but rather to explain how vein structures deformed and interacted under a variable stress field, characteristic of the subduction forearc region (Cerchiari et al., 2020; Dielforder et al., 2015; Magee & Zoback, 1993). (a) At a stage T_0, the principal compressive stress (σ_1) is oriented subperpendicular to the main shear plane (i.e., the subduction interface). In this scenario, extensional veins oriented (sub)parallel to σ_1 are formed and filled with high-pressure minerals. (b) Under new prevailing conditions (T_1), veins oriented at (c) 45° with respect to σ_1 will represent favorably oriented structures for slipping (see solid red lines), whereas those oriented at higher angles are misoriented. In either case, the veins represent preferential weaknesses in the rock volume. Thus, both favorably and unfavorably oriented veins can slip and be transposed, although favorably oriented veins are expected to form major slip planes. Moreover, extensional veins oriented parallel to σ_1 will be developed. (c) Further switching of the σ_1 orientation (at T_2 stage) would result in shearing along already brecciated and transposed veins. In this scenario, unfavorably oriented veins are capable of shearing, as they represent weaknesses associated with strain hardening processes. Due to shearing and transposition, vein structures and related discontinuities can merge or connect into main slip planes (see dashed red lines). (d) Overview of the subduction environment emphasizing how the occurrence of metamorphic vein networks potentially controls brittle creep localization in the deep episodic tremor and slip source region. The relevant metamorphic dehydration reactions—where significant volumes of fluids are expelled—as well as the source depths of LFEs for the Alaska, Costa Rica and Japan subduction zones are shown (relocated LFEs are from Brown et al. (2009, 2013) and Kato et al. (2010), respectively). Note that LFE locations do not necessarily match the temperatures inferred for each one of the subduction margins. Atg, antigorite; SST, slow slip and tremor; LFE, low-frequency earthquake; Pref., preferential; press., pressure.

studied here were crosscut at near-peak conditions by massive aragonite-precipitating hydrofracturing events (the third vein set described above; Muñoz-Montecinos, Angiboust, Garcia-Casco, Glodny, & Bebout, 2021). The greater abundance of hydraulic breccias (i.e., the aragonite-bearing veins) forming toward the base of the SST region could represent a potential source of deep tremor associated with hydrofracturing rather than shear slip (Shapiro et al., 2018). Thus, from a geological perspective, the SST region might evolve along dip from a shallower tremor-genic source, characterized by localized slip and related ultracataclasites, to a deeper region dominated by massive tremor-genic hydrofracturing. Hence, fluid production from a deeper source and subsequent

updip-traveling fluid pulses (Frank et al., 2015; Muñoz-Montecinos, Angiboust, Garcia-Casco, Glodny, & Bebout, 2021) might represent a model for explaining spatial-temporal Vp/Vs variations (Gosselin et al., 2020), as well as seismological observations reporting fast tremor migration and bimodal deep tectonic tremor distribution in active margins (Cruz-Atienza et al., 2018; Frank et al., 2015; Kato et al., 2010; Sawaki et al., 2021).

8. Conclusions

We performed a petro-structural investigation onto the lawsonite-bearing veins and their surrounding blueschist host exposed now in the Zagros suture (southeastern Iran). Our meso- and micro-structural observations demonstrate that the veins bear evidence suggesting brittle creep as a dominant deformation mechanism active at high-pressure. Such conditions are compatible with the depth range (30–55 km) at which a variety of seismic and aseismic processes occur in active subduction margins (e.g., slow slips and tremors). We emphasize that cataclastic fabrics are typically found in the immediate vicinity of veins (i.e., at the host-vein margins), while sets of extensional veins commonly develop into localized shear bands. Major and trace elements distribution reveal that (ultra)cataclastic host-vein margins are enriched up to 12 times in Ti, Ta, Nb and Zr (i.e., HFSEs) as well as in Cr compared to the pristine blueschist host. On the other hand, the light rare earth elements are depleted in two orders of magnitude. Similar chemical anomalies occur in the form of mineral zoning patterns in brecciated lawsonite vein crystals. These results are therefore interpreted as reflecting the chemical fingerprint of open system fluid circulation associated with the injection of fluid pulses originating from a deep-seated, mafic/ultramafic-derived, external source. We conclude that the mechanical effects of metamorphic fluids are twofold: (a) they produce rheological heterogeneities in the form of mineral-filled extensional veins that are, in general, stiffer than the surrounding host; and (b) they transiently decrease the effective normal stress and the strength of the subduction interface inducing brittle creep along vein margins. Thus, the combined effects of fluids and veins could generate a favorable scenario for SSTs nucleation and propagation, controlling slip localization along deep subduction interfaces.

Data Availability Statement

The GPS location of the samples and raw LA-ICP-MS results are publicly available in the ETH Research Collection repositories (this data is accessible in https://doi.org/10.3929/ethz-b-000603012; Tables S1 and S2, respectively).

References

Agard, P., Monié, P., Gerber, W., Omrani, J., Molinaro, M., Meyer, B., et al. (2006). Transient, synobduction exhumation of Zagros blueschists inferred from P-T, deformation, time, and kinematic constraints: Implications for Neotethyan wedge dynamics. *Journal of Geophysical Research*, *111*(B11). https://doi.org/10.1029/2005jb004103

Alavi, M. (1994). Tectonics of the Zagros orogenic belt of Iran: New data and interpretations. *Tectonophysics*, *229*(3–4), 211–238. https://doi.org/10.1016/0040-1951(94)90030-2

Angiboust, S., Agard, P., Glodny, J., Omrani, J., & Oncken, O. (2016). Zagros blueschists: Episodic underplating and long-lived cooling of a subduction zone. *Earth and Planetary Science Letters*, *443*, 48–58. https://doi.org/10.1016/j.epsl.2016.03.017

Angiboust, S., Kirsch, J., Oncken, O., Glodny, J., Monié, P., & Rybacki, E. (2015). Probing the transition between seismically coupled and decoupled segments along an ancient subduction interface. *Geochemistry, Geophysics, Geosystems*, *16*(6), 1905–1922. https://doi.org/10.1002/2015gc005776

Angiboust, S., Muñoz-Montecinos, J., Cambeses, A., Raimondo, T., Deldicque, D., & Garcia-Casco, A. (2021). Jolts in the Jade factory: A route for subduction fluids and their implications for mantle wedge seismicity. *Earth-Science Reviews*, *220*, 103720. https://doi.org/10.1016/j.earscirev.2021.103720

Angiboust, S., Pettke, T., De Hoog, J. C., Caron, B., & Oncken, O. (2014). Channelized fluid flow and eclogite-facies metasomatism along the subduction shear zone. *Journal of Petrology*, *55*(5), 883–916. https://doi.org/10.1093/petrology/egu010

Angiboust, S., & Raimondo, T. (2022). Permeability of subducted oceanic crust revealed by eclogite-facies vugs. *Geology*, *50*(8), 964–968. https://doi.org/10.1130/g50066.1

Angiboust, S., Yamato, P., Hertgen, S., Hyppolito, T., Bebout, G. E., & Morales, L. (2017). Fluid pathways and high-P metasomatism in a subducted continental slice (Mt. Emilius klippe, W. Alps). *Journal of Metamorphic Geology*, *35*(5), 471–492. https://doi.org/10.1111/jmg.12241

Arvin, M., Pan, Y., Dargahi, S., Malekizadeh, A., & Babaei, A. (2007). Petrochemistry of the Siah-Kuh granitoid stock southwest of Kerman, Iran: Implications for initiation of Neotethys subduction. *Journal of Asian Earth Sciences*, *30*(3–4), 474–489. https://doi.org/10.1016/j.jseaes.2007.01.001

Audet, P., & Kim, Y. (2016). Teleseismic constraints on the geological environment of deep episodic slow earthquakes in subduction zone forearcs: A review. *Tectonophysics*, *670*, 1–15. https://doi.org/10.1016/j.tecto.2016.01.005

Barker, S. L., Cox, S. F., Eggins, S. M., & Gagan, M. K. (2006). Microchemical evidence for episodic growth of antitaxial veins during fracture-controlled fluid flow. *Earth and Planetary Science Letters*, *250*(1–2), 331–344. https://doi.org/10.1016/j.epsl.2006.07.051

Bassett, D., & Watts, A. B. (2015). Gravity anomalies, crustal structure, and seismicity at subduction zones: 2. Interrelationships between fore-arc structure and seismogenic behavior. *Geochemistry, Geophysics, Geosystems*, *16*(5), 1541–1576. https://doi.org/10.1002/2014gc005685

Beall, A., Fagereng, Å., & Ellis, S. (2019). Strength of strained two-phase mixtures: Application to rapid creep and stress amplification in subduction zone mélange. *Geophysical Research Letters*, *46*(1), 169–178. https://doi.org/10.1029/2018gl081252

Bebout, G. E., & Barton, M. D. (1993). Metasomatism during subduction: Products and possible paths in the Catalina Schist, California. *Chemical Geology*, *108*(1–4), 61–92. https://doi.org/10.1016/0009-2541(93)90318-d

Behr, W. M., & Bürgmann, R. (2021). What's down there? The structures, materials and environment of deep-seated slow slip and tremor. *Philosophical Transactions of the Royal Society A*, *379*(2193), 20200218. https://doi.org/10.1098/rsta.2020.0218

Behr, W. M., Kotowski, A. J., & Ashley, K. T. (2018). Dehydration-induced rheological heterogeneity and the deep tremor source in warm subduction zones. *Geology*, *46*(5), 475–478. https://doi.org/10.1130/g40105.1

Bonnet, G., Agard, P., Whitechurch, H., Fournier, M., Angiboust, S., Caron, B., & Omrani, J. (2020). Fossil seamount in southeast Zagros records intraoceanic arc to back-arc transition: New constraints for the evolution of the Neotethys. *Gondwana Research*, *81*, 423–444. https://doi.org/10.1016/j.gr.2019.10.019

Bons, P. D., Elburg, M. A., & Gomez-Rivas, E. (2012). A review of the formation of tectonic veins and their microstructures. *Journal of Structural Geology*, *43*, 33–62. https://doi.org/10.1016/j.jsg.2012.07.005

Bostock, M. G., Thomas, A. M., Savard, G., Chuang, L., & Rubin, A. M. (2015). Magnitudes and moment-duration scaling of low-frequency earthquakes beneath southern Vancouver Island. *Journal of Geophysical Research: Solid Earth*, *120*(9), 6329–6350. https://doi.org/10.1002/2015jb012195

Braden, Z., & Behr, W. M. (2021). Weakening mechanisms in a basalt-hosted subduction megathrust fault segment, southern Alaska. *Journal of Geophysical Research: Solid Earth*, *126*(9), e2021JB022039. https://doi.org/10.1029/2021jb022039

Brady, J. B. (1975). Chemical components and diffusion. *American Journal of Science*, *275*(9), 1073–1088. https://doi.org/10.2475/ajs.275.9.1073

Brown, J. R., Beroza, G. C., Ide, S., Ohta, K., Shelly, D. R., Schwartz, S. Y., et al. (2009). Deep low-frequency earthquakes in tremor localize to the plate interface in multiple subduction zones. *Geophysical Research Letters*, *36*(19), L19306. https://doi.org/10.1029/2009gl040027

Brown, J. R., Prejean, S. G., Beroza, G. C., Gomberg, J. S., & Haeussler, P. J. (2013). Deep low-frequency earthquakes in tectonic tremor along the Alaska-Aleutian subduction zone. *Journal of Geophysical Research: Solid Earth*, *118*(3), 1079–1090. https://doi.org/10.1029/2012jb009459

Cao, Y., Jung, H., & Song, S. (2014). Microstructures and petro-fabrics of lawsonite blueschist in the North Qilian suture zone, NW China: Implications for seismic anisotropy of subducting oceanic crust. *Tectonophysics*, *628*, 140–157. https://doi.org/10.1016/j.tecto.2014.04.028

Cárdenas-Párraga, J., Garcia-Casco, A., Blanco-Quintero, I. F., Rojas-Agramonte, Y., Cambra, K. N., & Harlow, G. E. (2021). A Highly dynamic hot hydrothermal system in the subduction environment: Geochemistry and geochronology of jadeitite and associated rocks of the Sierra del Convento mélange (eastern Cuba). *American Journal of Science*, *321*(6), 822–887. https://doi.org/10.2475/06.2021.06

Ceccato, A., Pennacchioni, G., Menegon, L., & Bestmann, M. (2017). Crystallographic control and texture inheritance during mylonitization of coarse grained quartz veins. *Lithos*, *290*, 210–227. https://doi.org/10.1016/j.lithos.2017.08.005

Cerchiari, A., Remitti, F., Mittempergher, S., Festa, A., Lugli, F., & Cipriani, A. (2020). Cyclical variations of fluid sources and stress state in a shallow megathrust-zone mélange. *Journal of the Geological Society*, *177*(3), 647–659. https://doi.org/10.1144/jgs2019-072

Collettini, C., Niemeijer, A., Viti, C., & Marone, C. (2009). Fault zone fabric and fault weakness. *Nature*, *462*(7275), 907–910. https://doi.org/10.1038/nature08585

Cruz-Atienza, V. M., Villafuerte, C., & Bhat, H. S. (2018). Rapid tremor migration and pore-pressure waves in subduction zones. *Nature Communications*, *9*(1), 1–13. https://doi.org/10.1038/s41467-018-05150-3

Dal Zilio, L., & Gerya, T. (2022). Subduction earthquake cycles controlled by episodic fluid pressure cycling. *Lithos*, *426*, 106800. https://doi.org/10.1016/j.lithos.2022.106800

Delph, J. R., Levander, A., & Niu, F. (2018). Fluid controls on the heterogeneous seismic characteristics of the Cascadia margin. *Geophysical Research Letters*, *45*(20), 11–021. https://doi.org/10.1029/2018gl079518

Dielforder, A., Vollstaedt, H., Vennemann, T., Berger, A., & Herwegh, M. (2015). Linking megathrust earthquakes to brittle deformation in a fossil accretionary complex. *Nature Communications*, *6*(1), 7504. https://doi.org/10.1038/ncomms8504

Evans, B. W. (1990). Phase relations of epidote-blueschists. *Lithos*, *25*(1–3), 3–23. https://doi.org/10.1016/0024-4937(90)90003-j

Fabbri, O., Goldsby, D. L., Chester, F., Karpoff, A. M., Morvan, G., Ujiie, K., et al. (2020). Deformation structures from splay and décollement faults in the Nankai accretionary prism, SW Japan (IODP NanTroSEIZE Expedition 316): Evidence for slow and rapid slip in fault rocks. *Geochemistry, Geophysics, Geosystems*, *21*(6), e2019GC008786. https://doi.org/10.1029/2019gc008786

Fagereng, Å., Remitti, F., & Sibson, R. H. (2010). Shear veins observed within anisotropic fabric at high angles to the maximum compressive stress. *Nature Geoscience*, *3*(7), 482–485. https://doi.org/10.1038/ngeo898

Fagereng, Å., & Sibson, R. H. (2010). Melange rheology and seismic style. *Geology*, *38*(8), 751–754. https://doi.org/10.1130/g30868.1

Fisher, D. M., & Brantley, S. L. (1992). Models of quartz overgrowth and vein formation: Deformation and episodic fluid flow in an ancient subduction zone. *Journal of Geophysical Research*, *97*(B13), 20043–20061. https://doi.org/10.1029/92jb01582

Frank, W. B., Shapiro, N. M., Husker, A. L., Kostoglodov, V., Bhat, H. S., & Campillo, M. (2015). Along-fault pore-pressure evolution during a slow-slip event in Guerrero, Mexico. *Earth and Planetary Science Letters*, *413*, 135–143. https://doi.org/10.1016/j.epsl.2014.12.051

Fry, B., Chao, K., Bannister, S., Peng, Z., & Wallace, L. (2011). Deep tremor in New Zealand triggered by the 2010 Mw8. 8 Chile earthquake. *Geophysical Research Letters*, *38*(15), L15306. https://doi.org/10.1029/2011gl048319

Fu, Y., & Freymueller, J. T. (2013). Repeated large slow slip events at the southcentral Alaska subduction zone. *Earth and Planetary Science Letters*, *375*, 303–311. https://doi.org/10.1016/j.epsl.2013.05.049

Gao, J., John, T., Klemd, R., & Xiong, X. (2007). Mobilization of Ti–Nb–Ta during subduction: Evidence from rutile-bearing dehydration segregations and veins hosted in eclogite, Tianshan, NW China. *Geochimica et Cosmochimica Acta*, *71*(20), 4974–4996. https://doi.org/10.1016/j.gca.2007.07.027

Ghasemi, H., Juteau, T., Bellon, H., Sabzehei, M., Whitechurch, H., & Ricou, L. E. (2002). The mafic–ultramafic complex of Sikhoran (central Iran): A polygenetic ophiolite complex. *Comptes Rendus Geoscience*, *334*(6), 431–438. https://doi.org/10.1016/s1631-0713(02)01770-4

Giuntoli, F., Menegon, L., & Warren, C. J. (2018). Replacement reactions and deformation by dissolution and precipitation processes in amphibolites. *Journal of Metamorphic Geology*, *36*(9), 1263–1286. https://doi.org/10.1111/jmg.12445

Giuntoli, F., & Viola, G. (2022). A likely geological record of deep tremor and slow slip events from a subducted continental broken formation. *Scientific Reports*, *12*(1), 1–14. https://doi.org/10.1038/s41598-022-08489-2

Giuntoli, F., Viola, G., & Sørensen, B. E. (2022). Deformation mechanisms of blueschist facies continental metasediments may offer insights into deep episodic tremor and slow slip events. *Journal of Geophysical Research: Solid Earth*, *127*(10), e2022JB024265. https://doi.org/10.1029/2022jb024265

Gosselin, J. M., Audet, P., Estève, C., McLellan, M., Mosher, S. G., & Schaeffer, A. J. (2020). Seismic evidence for megathrust fault-valve behavior during episodic tremor and slip. *Science Advances*, *6*(4), eaay5174. https://doi.org/10.1126/sciadv.aay5174

Hassanzadeh, J., & Wernicke, B. P. (2016). The Neotethyan Sanandaj-Sirjan zone of Iran as an archetype for passive margin-arc transitions. *Tectonics*, *35*(3), 586–621. https://doi.org/10.1002/2015tc003926

Holtmann, R., Muñoz-Montecinos, J., Angiboust, S., Cambeses, A., Bonnet, G., Brown, A., et al. (2022). Cretaceous thermal evolution of the closing Neo-Tethyan realm revealed by multi-method petrochronology. *Lithos*, *422–423*, 106731. https://doi.org/10.1016/j.lithos.2022.106731

Hyndman, R. D., McCrory, P. A., Wech, A., Kao, H., & Ague, J. (2015). Cascadia subducting plate fluids channelled to fore-arc mantle corner: ETS and silica deposition. *Journal of Geophysical Research: Solid Earth*, *120*(6), 4344–4358. https://doi.org/10.1002/2015jb011920

Ide, S., Beroza, G. C., Shelly, D. R., & Uchide, T. (2007). A scaling law for slow earthquakes. *Nature*, *447*(7140), 76–79. https://doi.org/10.1038/nature05780

Ildefonse, B., Lardeaux, J. M., & Caron, J. M. (1990). The behavior of shape preferred orientations in metamorphic rocks: Amphiboles and jadeites from the Monte Mucrone area (Sesia-Lanzo zone, Italian Western Alps). *Journal of Structural Geology*, *12*(8), 1005–1011. https://doi.org/10.1016/0191-8141(90)90096-h

Imon, R., Okudaira, T., & Kanagawa, K. (2004). Development of shape-and lattice-preferred orientations of amphibole grains during initial cataclastic deformation and subsequent deformation by dissolution–precipitation creep in amphibolites from the Ryoke metamorphic belt, SW Japan. *Journal of Structural Geology*, *26*(5), 793–805. https://doi.org/10.1016/j.jsg.2003.09.004

Kananian, A., Sarjoughian, F., Nadimi, A., Ahmadian, J., & Ling, W. (2014). Geochemical characteristics of the Kuh-e Dom intrusion, Urumieh–Dokhtar Magmatic Arc (Iran): Implications for source regions and magmatic evolution. *Journal of Asian Earth Sciences*, *90*, 137–148. https://doi.org/10.1016/j.jseaes.2014.04.026

Kato, A., Iidaka, T., Ikuta, R., Yoshida, Y., Katsumata, K., Iwasaki, T., et al. (2010). Variations of fluid pressure within the subducting oceanic crust and slow earthquakes. *Geophysical Research Letters*, *37*(14), L14310. https://doi.org/10.1029/2010gl043723

Kay, M. A., Main, I. G., Elphick, S. C., & Ngwenya, B. T. (2006). Fault gouge diagenesis at shallow burial depth: Solution–precipitation reactions in well-sorted and poorly sorted powders of crushed sandstone. *Earth and Planetary Science Letters*, *243*(3–4), 607–614. https://doi.org/10.1016/j.epsl.2006.01.017

Kim, D., Katayama, I., Wallis, S., Michibayashi, K., Miyake, A., Seto, Y., & Azuma, S. (2015). Deformation microstructures of glaucophane and lawsonite in experimentally deformed blueschists: Implications for intermediate-depth intraplate earthquakes. *Journal of Geophysical Research: Solid Earth*, *120*(2), 1229–1242. https://doi.org/10.1002/2014jb011528

Kirkpatrick, J. D., Fagereng, Å., & Shelly, D. R. (2021). Geological constraints on the mechanisms of slow earthquakes. *Nature Reviews Earth & Environment*, *2*(4), 285–301. https://doi.org/10.1038/s43017-021-00148-w

Kjøll, H. J., Viola, G., Menegon, L., & Sørensen, B. E. (2015). Brittle–viscous deformation of vein quartz under fluid-rich lower greenschist facies conditions. *Solid Earth*, *6*(2), 681–699. https://doi.org/10.5194/se-6-681-2015

Kotowski, A. J., & Behr, W. M. (2019). Length scales and types of heterogeneities along the deep subduction interface: Insights from exhumed rocks on Syros Island, Greece. *Geosphere*, *15*(4), 1038–1065. https://doi.org/10.1130/ges02037.1

Lai, P., Moulton, K., & Krevor, S. (2015). Pore-scale heterogeneity in the mineral distribution and reactive surface area of porous rocks. *Chemical Geology*, *411*, 260–273. https://doi.org/10.1016/j.chemgeo.2015.07.010

Leeman, J. R., Saffer, D. M., Scuderi, M. M., & Marone, C. (2016). Laboratory observations of slow earthquakes and the spectrum of tectonic fault slip modes. *Nature Communications*, *7*(1), 1–6. https://doi.org/10.1038/ncomms11104

Liferovich, R. P., & Mitchell, R. H. (2005). Composition and paragenesis of Na-Nb-and Zr-bearing titanite from Khibina, Russia, and crystal-structure data for synthetic analogues. *The Canadian Mineralogist*, *43*(2), 795–812. https://doi.org/10.2113/gscanmin.43.2.795

Magee, M. E., & Zoback, M. D. (1993). Evidence for a weak interplate thrust fault along the northern Japan subduction zone and implications for the mechanics of thrust faulting and fluid expulsion. *Geology*, *21*(9), 809–812. https://doi.org/10.1130/0091-7613(1993)021<0809:efawit>2.3.co;2

McLellan, M., Audet, P., Rosas, J. C., & Currie, C. (2022). Margin-wide variations in slab dehydration in Cascadia and their relationship to slow slip. *Lithos*, *434*, 106912. https://doi.org/10.1016/j.lithos.2022.106912

Meneghini, F., & Moore, J. C. (2007). Deformation and hydrofracture in a subduction thrust at seismogenic depths: The Rodeo Cove thrust zone, Marin Headlands, California. *Geological Society of America Bulletin*, *119*(1–2), 174–183. https://doi.org/10.1130/b25807.1

Menegon, L., Pennacchioni, G., Heilbronner, R., & Pittarello, L. (2008). Evolution of quartz microstructure and *c*-axis crystallographic preferred orientation within ductilely deformed granitoids (Arolla unit, Western Alps). *Journal of Structural Geology*, *30*(11), 1332–1347. https://doi.org/10.1016/j.jsg.2008.07.007

Misch, P. (1969). Paracrystalline microboudinage of zoned grains and other criteria for synkinematic growth of metamorphic minerals. *American Journal of Science*, *267*(1), 43–63. https://doi.org/10.2475/ajs.267.1.43

Morales, L. F., Lloyd, G. E., & Mainprice, D. (2014). Fabric transitions in quartz via viscoplastic self-consistent modeling part I: Axial compression and simple shear under constant strain. *Tectonophysics*, *636*, 52–69. https://doi.org/10.1016/j.tecto.2014.08.011

Muñoz-Montecinos, J., Angiboust, S., Cambeses, A., & García-Casco, A. (2020). Multiple veining in a paleo–accretionary wedge: The metamorphic rock record of prograde dehydration and transient high pore-fluid pressures along the subduction interface (Western Series, central Chile). *Geosphere*, *16*(3), 765–786. https://doi.org/10.1130/ges02227.1

Muñoz-Montecinos, J., Angiboust, S., & Garcia-Casco, A. (2021). Blueschist-facies paleo-earthquakes in a serpentinite channel (Zagros suture, Iran) enlighten seismogenesis in Mariana-type subduction margins. *Earth and Planetary Science Letters*, *573*, 117135. https://doi.org/10.1016/j.epsl.2021.117135

Muñoz-Montecinos, J., Angiboust, S., Garcia-Casco, A., Glodny, J., & Bebout, G. (2021). Episodic hydrofracturing and large-scale flushing along deep subduction interfaces: Implications for fluid transfer and carbon recycling (Zagros Orogen, southeastern Iran). *Chemical Geology*, *571*, 120173. https://doi.org/10.1016/j.chemgeo.2021.120173

Obara, K., & Kato, A. (2016). Connecting slow earthquakes to huge earthquakes. *Science*, *353*(6296), 253–257. https://doi.org/10.1126/science.aaf1512

Oberhänsli, R., Bousquet, R., Moinzadeh, H., Moazzen, M., & Arvin, M. (2007). The field of stability of blue jadeite: A new occurrence of jadeitite at Sorkhan, Iran, as a case study. *The Canadian Mineralogist*, *45*(6), 1501–1509. https://doi.org/10.3749/canmin.45.6.1501

Oncken, O., Angiboust, S., & Dresen, G. (2022). Slow slip in subduction zones: Reconciling deformation fabrics with instrumental observations and laboratory results. *Geosphere*, *18*(1), 104–129. https://doi.org/10.1130/ges02382.1

Padrón-Navarta, J. A., Sánchez-Vizcaíno, V. L., Hermann, J., Connolly, J. A., Garrido, C. J., Gómez-Pugnaire, M. T., & Marchesi, C. (2013). Tschermak's substitution in antigorite and consequences for phase relations and water liberation in high-grade serpentinites. *Lithos*, *178*, 186–196. https://doi.org/10.1016/j.lithos.2013.02.001

Park, Y., Jung, S., & Jung, H. (2020). Lattice preferred orientation and deformation microstructures of glaucophane and epidote in experimentally deformed epidote blueschist at high pressure. *Minerals*, *10*(9), 803. https://doi.org/10.3390/min10090803

Peacock, S. M. (2009). Thermal and metamorphic environment of subduction zone episodic tremor and slip. *Journal of Geophysical Research*, *114*(B8), B00A07. https://doi.org/10.1029/2008jb005978

Rogers, G., & Dragert, H. (2003). Episodic tremor and slip on the Cascadia subduction zone: The chatter of silent slip. *Science*, *300*(5627), 1942–1943. https://doi.org/10.1126/science.1084783

Rowe, C. D., & Griffith, W. A. (2015). Do faults preserve a record of seismic slip: A second opinion. *Journal of Structural Geology*, *78*, 1–26. https://doi.org/10.1016/j.jsg.2015.06.006

Rowe, C. D., Meneghini, F., & Moore, J. C. (2011). Textural record of the seismic cycle: Strain-rate variation in an ancient subduction thrust. *Geological Society, London, Special Publications*, *359*(1), 77–95. https://doi.org/10.1144/sp359.5

Rubin, A. M., & Armbruster, J. G. (2013). Imaging slow slip fronts in Cascadia with high precision cross-station tremor locations. *Geochemistry, Geophysics, Geosystems*, *14*(12), 5371–5392. https://doi.org/10.1002/2013gc005031

Sabzehei, M. (1974). *Les Mélanges ophiolitiques de la région d'Esfandagheh (Iran méridional): Étude pétrologique et structurale, interprétation dans le cadre iranien* (Doctoral dissertation).Université Scientifique et Médicale de Grenoble.

Saffer, D. M. (2014). The permeability of active subduction plate boundary faults. *Geofluids*, *15*(1–2), 193–215. https://doi.org/10.1111/gfl.12103

Sawaki, Y., Ito, Y., Ohta, K., Shibutani, T., & Iwata, T. (2021). Seismological structures on bimodal distribution of deep tectonic tremor. *Geophysical Research Letters*, *48*(8), e2020GL092183. https://doi.org/10.1029/2020gl092183

Schrank, C. E., Handy, M. R., & Fusseis, F. (2008). Multiscaling of shear zones and the evolution of the brittle-to-viscous transition in continental crust. *Journal of Geophysical Research*, *113*(B1), B01407. https://doi.org/10.1029/2006jb004833

Shapiro, N. M., Campillo, M., Kaminski, E., Vilotte, J. P., & Jaupart, C. (2018). Low-frequency earthquakes and pore pressure transients in subduction zones. *Geophysical Research Letters*, *45*(20), 11–083. https://doi.org/10.1029/2018gl079893

Shelly, D. R., Beroza, G. C., Ide, S., & Nakamula, S. (2006). Low-frequency earthquakes in Shikoku, Japan, and their relationship to episodic tremor and slip. *Nature*, *442*(7099), 188–191. https://doi.org/10.1038/nature04931

Sibson, R. H. (2013). Stress switching in subduction forearcs: Implications for overpressure containment and strength cycling on megathrusts. *Tectonophysics*, *600*, 142–152. https://doi.org/10.1016/j.tecto.2013.02.035

Sibson, R. H., Robert, F., & Poulsen, K. H. (1988). High-angle reverse faults, fluid-pressure cycling, and mesothermal gold-quartz deposits. *Geology*, *16*(6), 551–555. https://doi.org/10.1130/0091-7613(1988)016<0551:harffp>2.3.co;2

Sorensen, S. S., & Grossman, J. N. (1989). Enrichment of trace elements in garnet amphibolites from a paleo-subduction zone: Catalina Schist, southern California. *Geochimica et Cosmochimica Acta*, *53*(12), 3155–3177. https://doi.org/10.1016/0016-7037(89)90096-3

Spandler, C., Pettke, T., & Rubatto, D. (2011). Internal and external fluid sources for eclogite-facies veins in the Monviso meta-ophiolite, Western Alps: Implications for fluid flow in subduction zones. *Journal of Petrology*, *52*(6), 1207–1236. https://doi.org/10.1093/petrology/egr025

Stünitz, H., Gerald, J. F., & Tullis, J. (2003). Dislocation generation, slip systems, and dynamic recrystallization in experimentally deformed plagioclase single crystals. *Tectonophysics*, *372*(3–4), 215–233. https://doi.org/10.1016/s0040-1951(03)00241-5

Taetz, S., John, T., Bröcker, M., Spandler, C., & Stracke, A. (2018). Fast intraslab fluid-flow events linked to pulses of high pore fluid pressure at the subducted plate interface. *Earth and Planetary Science Letters*, *482*, 33–43. https://doi.org/10.1016/j.epsl.2017.10.044

Tarling, M. S., Smith, S. A., & Scott, J. M. (2019). Fluid overpressure from chemical reactions in serpentinite within the source region of deep episodic tremor. *Nature Geoscience*, *12*(12), 1034–1042. https://doi.org/10.1038/s41561-019-0470-z

Teyssier, C., Whitney, D. L., Toraman, E., & Seaton, N. C. (2010). Lawsonite vorticity and subduction kinematics. *Geology*, *38*(12), 1123–1126. https://doi.org/10.1130/g31409.1

Thomas, A. M., Nadeau, R. M., & Bürgmann, R. (2009). Tremor-tide correlations and near-lithostatic pore pressure on the deep San Andreas fault. *Nature*, *462*(7276), 1048–1051. https://doi.org/10.1038/nature08654

Trepmann, C. A., & Seybold, L. (2019). Deformation at low and high stress-loading rates. *Geoscience Frontiers*, *10*(1), 43–54. https://doi.org/10.1016/j.gsf.2018.05.002

Tribuzio, R., Messiga, B., Vannucci, R., & Bottazzi, P. (1996). Rare earth element redistribution during high-pressure–low-temperature metamorphism in ophiolitic Fe-gabbros (Liguria, northwestern Italy): Implications for light REE mobility in subduction zones. *Geology*, *24*(8), 711–714. https://doi.org/10.1130/0091-7613(1996)024<0711:reerdh>2.3.co;2

Ujiie, K., Saishu, H., Fagereng, Å., Nishiyama, N., Otsubo, M., Masuyama, H., & Kagi, H. (2018). An explanation of episodic tremor and slow slip constrained by crack-seal veins and viscous shear in subduction mélange. *Geophysical Research Letters*, *45*(11), 5371–5379. https://doi.org/10.1029/2018gl078374

Vignaroli, G., Rossetti, F., Billi, A., Theye, T., & Belardi, G. (2020). Structurally controlled growth of fibrous amphibole in tectonized metagabbro: Constraints on asbestos concentrations in non-serpentinized rocks. *Journal of the Geological Society*, *177*(1), 103–119. https://doi.org/10.1144/jgs2018-235

Vitale Brovarone, A., Alard, O., Beyssac, O., Martin, L., & Picatto, M. (2014). Lawsonite metasomatism and trace element recycling in subduction zones. *Journal of Metamorphic Geology*, *32*(5), 489–514. https://doi.org/10.1111/jmg.12074

Wang, K., Huang, T., Tilmann, F., Peacock, S. M., & Lange, D. (2020). Role of Serpentinized mantle wedge in affecting Megathrust Seismogenic behavior in the area of the 2010 M= 8.8 Maule earthquake. *Geophysical Research Letters*, *47*(22), e2020GL090482. https://doi.org/10.1029/2020gl090482

Wannamaker, P. E., Evans, R. L., Bedrosian, P. A., Unsworth, M. J., Maris, V., & McGary, R. S. (2014). Segmentation of plate coupling, fate of subduction fluids, and modes of arc magmatism in Cascadia, inferred from magnetotelluric resistivity. *Geochemistry, Geophysics, Geosystems*, *15*(11), 4230–4253. https://doi.org/10.1002/2014gc005509

Warren-Smith, E., Fry, B., Wallace, L., Chon, E., Henrys, S., Sheehan, A., et al. (2019). Episodic stress and fluid pressure cycling in subducting oceanic crust during slow slip. *Nature Geoscience*, *12*(6), 475–481. https://doi.org/10.1038/s41561-019-0367-x

Wassmann, S., & Stöckhert, B. (2012). Matrix deformation mechanisms in HP-LT tectonic mélanges—Microstructural record of jadeite blueschist from the Franciscan Complex, California. *Tectonophysics*, *568*, 135–153. https://doi.org/10.1016/j.tecto.2012.01.009

Whitney, D. L., Fornash, K. F., Kang, P., Ghent, E. D., Martin, L., Okay, A. I., & Brovarone, A. V. (2020). Lawsonite composition and zoning as tracers of subduction processes: A global review. *Lithos*, *370*, 105636. https://doi.org/10.1016/j.lithos.2020.105636

Williams, R. T., & Kirkpatrick, J. D. (2022). Are low-frequency earthquake Moments Area-or slip-limited? A rock record examination. *Geophysical Research Letters*, *49*(2), e2021GL095759. https://doi.org/10.1029/2021gl095759

Yamato, P., Duretz, T., & Angiboust, S. (2019). Brittle/ductile deformation of eclogites: Insights from numerical models. *Geochemistry, Geophysics, Geosystems*, *20*(7), 3116–3133. https://doi.org/10.1029/2019gc008249

References From the Supporting Information

Bachmann, F., Hielscher, R., & Schaeben, H. (2010). Texture analysis with MTEX–free and open source software toolbox. In *Solid state phenomena* (Vol. 160, pp. 63–68). Trans Tech Publications Ltd.

Bachmann, F., Hielscher, R., & Schaeben, H. (2011). Grain detection from 2d and 3d EBSD data—Specification of the MTEX algorithm. *Ultramicroscopy*, *111*(12), 1720–1733. https://doi.org/10.1016/j.ultramic.2011.08.002

García-Casco, A. (2007). Magmatic paragonite in trondhjemites from the Sierra del Convento mélange, Cuba. *American Mineralogist*, *92*(7), 1232–1237. https://doi.org/10.2138/am.2007.2598

Hellstrom, J., Paton, C., Woodhead, J., & Hergt, J. (2008). Iolite: Software for spatially resolved LA-(quad and MC) ICPMS analysis. *Mineralogical Association of Canada short course series*, *40*, 343–348.

Hielscher, R., & Schaeben, H. (2008). A novel pole figure inversion method: Specification of the MTEX algorithm. *Journal of Applied Crystallography*, *41*(6), 1024–1037. https://doi.org/10.1107/s0021889808030112

Hyppolito, T., Cambeses, A., Angiboust, S., Raimondo, T., García-Casco, A., & Juliani, C. (2019). Rehydration of eclogites and garnet-replacement processes during exhumation in the amphibolite facies. *Geological Society, London, Special Publications*, *478*(1), 217–239. https://doi.org/10.1144/sp478.3

Jochum, K. P., Weis, U., Stoll, B., Kuzmin, D., Yang, Q., Raczek, I., et al. (2011a). Determination of reference values for NIST SRM 610–617 glasses following ISO guidelines. *Geostandards and Geoanalytical Research*, *35*(4), 397–429. https://doi.org/10.1111/j.1751-908x.2011.00120.x

Jochum, K. P., Wilson, S. A., Abouchami, W., Amini, M., Chmeleff, J., Eisenhauer, A., et al. (2011b). GSD-1G and MPI-DING reference glasses for in situ and bulk isotopic determination. *Geostandards and Geoanalytical Research*, *35*(2), 193–226. https://doi.org/10.1111/j.1751-908x.2010.00114.x

Paton, C., Hellstrom, J., Paul, B., Woodhead, J., & Hergt, J. (2011). Iolite: Freeware for the visualisation and processing of mass spectrometric data. *Journal of Analytical Atomic Spectrometry*, *26*(12), 2508–2518. https://doi.org/10.1039/c1ja10172b

Pearce, N. J., Perkins, W. T., Westgate, J. A., Gorton, M. P., Jackson, S. E., Neal, C. R., & Chenery, S. P. (1997). A compilation of new and published major and trace element data for NIST SRM 610 and NIST SRM 612 glass reference materials. *Geostandards Newsletter*, *21*(1), 115–144. https://doi.org/10.1111/j.1751-908x.1997.tb00538.x

Raimondo, T., Payne, J., Wade, B., Lanari, P., Clark, C., & Hand, M. (2017). Trace element mapping by LA-ICP-MS: Assessing geochemical mobility in garnet. *Contributions to Mineralogy and Petrology*, *172*(4), 1–22. https://doi.org/10.1007/s00410-017-1339-z

Whitney, D. L., & Evans, B. W. (2010). Abbreviations for names of rock-forming minerals. *American Mineralogist*, *95*(1), 185–187. https://doi.org/10.2138/am.2010.3371

Woodhead, J. D., Hellstrom, J., Hergt, J. M., Greig, A., & Maas, R. (2007). Isotopic and elemental imaging of geological materials by laser ablation inductively coupled plasma-mass spectrometry. *Geostandards and Geoanalytical Research*, *31*(4), 331–343. https://doi.org/10.1111/j.1751-908x.2007.00104.x